Volume 46 | Number 24 | 21 December 2017 | Pages 7473–7842

Chem Soc Rev

Chemical Society Reviews
rsc.li/chem-soc-rev

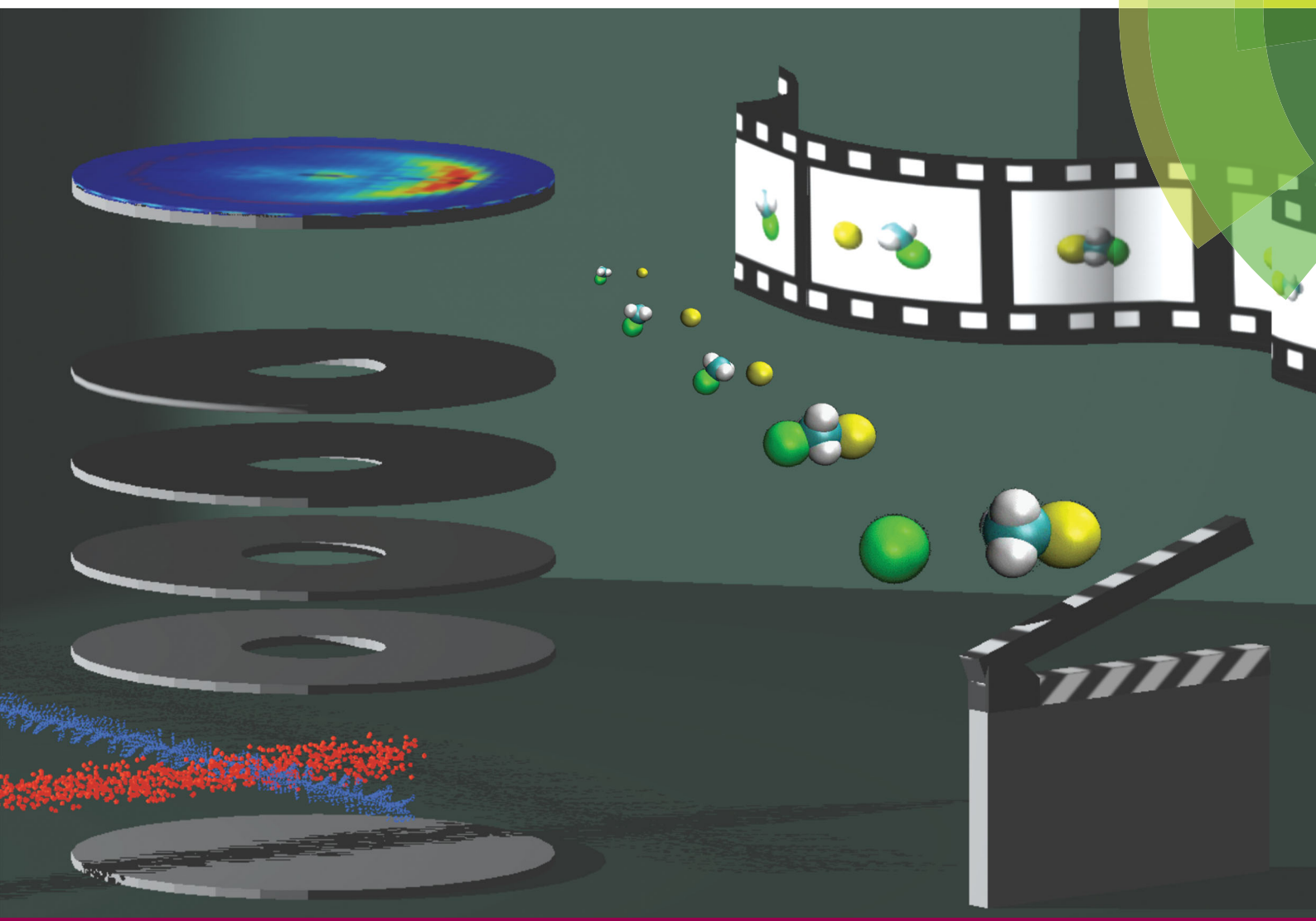

Includes a collection of articles on the theme of chemical reaction dynamics

ISSN 0306-0012

ROYAL SOCIETY OF CHEMISTRY

REVIEW ARTICLE
Roland Wester *et al.*
Imaging the dynamics of ion–molecule reactions

Chem Soc Rev

REVIEW ARTICLE

View Article Online
View Journal | View Issue

Cite this: *Chem. Soc. Rev.*, 2017, **46**, 7498

Received 22nd August 2017

DOI: 10.1039/c7cs00623c

rsc.li/chem-soc-rev

Imaging the dynamics of ion–molecule reactions

Eduardo Carrascosa, Jennifer Meyer and Roland Wester *

A range of ion–molecule reactions have been studied in the last years using the crossed-beam ion imaging technique, from charge transfer and proton transfer to nucleophilic substitution and elimination. This review presents the detailed insights that have been gained with respect to the dynamics of both cation–molecule and anion–molecule reactions studied with this method. In particular, we show the recent progress that has been achieved to understand the atomistic energetics and dynamics of ion–molecule reactions, such as the effects of vibrational quantum states, the formation of carbon–carbon bonds, and the competition between nucleophilic substitution and elimination.

Introduction

Ion–molecule reactions constitute an interdisciplinary research area that bridges chemistry and physics. This area has already attracted interest for many decades and still continues to rejuvenate itself. Ions are found in gaseous, liquid, and solid forms of matter, their spectral and collisional properties are therefore of interest for very different applications. In the gas phase, reactions of isolated ions with other neutral atoms or molecules are described by collisional cross sections that are much larger than usual neutral–neutral scattering cross sections.[1] The long-range interaction between the charge of the ion and the electrical polarizability, dipole or quadrupole moment of the neutral is responsible for this and renders ion–molecule reactions very important for the time evolution of ionized gases. The Earth's ionosphere, atmospheres of other planets or planetary satellites, and the gas clouds in the interstellar medium of our and other galaxies are important examples from our natural environment.[2–4] Plasma discharges used for semiconductor etching or tokamak plasmas and plasma-wall interactions in fusion research represent technical applications where ion–molecule reactions are important.[5] The temperatures at which ion–molecule reactions occur under these vastly different conditions range from few Kelvin in interstellar space to many thousands of Kelvin in atmospheric or technical plasmas.

It has already been known for the most part of the last century that gas phase reactions of ions with neutral atoms or molecules are important in weakly ionized media, such as the ionosphere. Many types of ion–molecule reactions have been identified and studied, but for many ion–molecule reactions that occur in our environment or in the interstellar medium detailed information on their reaction kinetics, product branching ratios, and reaction dynamics are still lacking. The simplest type of reaction, charge transfer, is often the starting point for chemical reaction networks, initiated when photon impact, cosmic ray ionization, or electron impact ionization creates a positively charged ion. Driven by the difference in ionization potential, this simple reaction can show intriguing features, because the ionization energy difference may be released to either product kinetic energy or to internal excitation depending on the details of the interaction potential. As discussed below for reactions of argon cations, this can also affect the total reaction cross section. Proton transfer and insertion reactions are other types of reactions that are frequently found for positively charged ions. For instance, interstellar chemistry is generally accepted to be initiated by reactions of the trihydrogen cation (H_3^+) with abundant interstellar atoms or molecules such as C, O, N_2 or CO.[6,7] These reactions open up different astrochemical networks that ultimately lead to aldehydes, carboxylic acids, amino acids *etc.*[8]

Anion–molecule reactions[9] are also important in many environments, in particular when the densities are high enough that free electrons can attach to neutrals to form negative ions, such as in the lower ionosphere of the Earth. Negative ions have also been found in the atmosphere of the moon Titan and in several interstellar molecular clouds, which has sparked a lot of interest in the formation and destruction of these anions. Negative ion reactions often feature a sizable potential barrier at short range, which can be attributed to electron–electron repulsion by electrostatic forces and the Pauli exclusion principle. Together with the long-range attractive interaction this leads to potential energy landscapes with two characteristic minima along the reaction coordinate. A range of reaction types are found for negative ions, such as associative detachment, nucleophilic substitution, and base-induced elimination. The dynamics of such reactions are discussed below.

Institut für Ionenphysik und Angewandte Physik, Universität Innsbruck, Technikerstraße 25, 6020 Innsbruck, Austria. E-mail: roland.wester@uibk.ac.at; Tel: +43 512 507 52620

The primary interest in an ion–molecule reaction is usually the total reaction cross section or rate coefficient. Several experimental techniques have been developed to measure ion–molecule reaction rate coefficients as a function of temperature or collision energy and investigate how they compare to the classical Langevin or capture cross section.[10,11] Widely used techniques to measure ion–molecule reaction kinetics are selected ion flow tubes,[12] guided ion beams,[13] supersonic flows (CRESU),[14] or radiofrequency ion trapping.[15] Recently, the combination of ion and neutral atom cooling and trapping has opened up an active field studying ultracold ion-atom collisions.[16]

To understand in detail why and how a reaction occurs, one has to move beyond the total reaction cross section and investigate the reaction dynamics. This is the topic of the present review. The term dynamics in general refers to the characteristics that describe how a set of reactants evolve into product atoms or molecules.[11] In the time-dependent description of quantum mechanics, the dynamics can be described by a multidimensional molecular wavepacket that is initialized at the reactants and evolves into products. In the equivalent time-independent description, the dynamics are described by the fully differential reactive scattering cross section, which depends on the internal quantum states of all reactants and products, on the relative velocity, and on the initial and final orbital angular momentum. Experimentally, neither the full time-dependent nor time-independent dynamics can be observed with state-of-the art techniques. In practice, many reaction dynamics experiments probe the time-independent differential scattering cross section as a function of initial and final velocity and scattering angle. Additional control of the internal quantum states of the reactants is exerted as far as can be achieved. In this review, the dynamics of ion–molecule reactions are discussed as obtained from crossed-beam studies with the velocity map imaging technique.[17] In principle, also direct femtosecond pump–probe experiments on chemical reactions can be performed, but there the reactants have to be already in close proximity when a pump pulse initiates the dynamics.[18–20]

Reaction dynamics are driven by the interaction potential, usually the relevant Born–Oppenheimer potential hypersurface or several coupled hypersurfaces. For ion–molecule reactions, the interaction is strongly attractive at large reactant separations and leads to deep energy minima that may or may not show one or several barriers at short internuclear separation. Such barriers, even if they are energetically below the energy of the reactants can have a profound influence on the dynamics. Furthermore, the dwell time of the reaction complex in the energy minima and the statistical or non-statistical coupling among the rovibrational degrees of freedom change the reaction dynamics and the branching into different open product channels. All these aspects can depend on the translational energy and the thermal or non-thermal excitation of internal quantum states of the reactants.

To experimentally unravel reaction dynamics, crossed-beam reactive scattering experiments have been performed in the past on a number of ion–molecule reactions using the rotatable detector technique.[21] Furthermore, the guided-ion-beam technique was employed to extract total and differential scattering cross sections.[22] These studies focused mostly on three- or four-atom reactions, where the count rates of the experiments and the preparation of reactant ion beams did not pose severe limitations. The development of the velocity map imaging (VMI) technique[17,23] has changed this and offered a substantially improved method to measure product differential scattering cross sections. A VMI spectrometer acts as a detector with a 4π solid angle of acceptance, which improves the detection efficiency for reaction products by orders of magnitude compared to a rotatable detector. It also decouples sensitivity and angular resolution.[24,25] Examples for crossed-beam scattering experiments for neutral molecules that have exploited the VMI technique are studies of the H + D_2 reaction[26] or reactions of F, Cl and O with CH_4.[27–29]

The first application of velocity map imaging to study ion–molecule reactive scattering came in 2002 by Weisshaar and co-workers, who studied reactions of cobalt cations with different hydrocarbon molecules. In their experiment the cations were created by pulsed laser ionization directly in the interaction region.[30] In the experiment that we have set up a few years later a spatially separated ion source was employed,[31] which had also been the concept used in previous experiments employing rotatable detectors. This yields a lot of flexibility to create and control different ionic species, in particular also negative ions. In addition our setup includes a radiofrequency ion trap[15,32] to pre-cool the ions prior to crossing the neutral reactant beam. This facilitates the reduction of the collision energy spread down to about 200 meV (FWHM) and allows for the preparation of internally cold molecular ions.[32] Our velocity map imaging spectrometer, which incorporates correlated position and arrival time measurements to determine three-dimensional product velocity distributions, has been described in detail in previous publications.[33–37] We therefore do not present the experimental method in this review. In the ion–molecule imaging experimental setup by Farrar and co-workers a versatile ion beam is combined with a supersonic beam source that is also equipped to produce neutral radicals. Scattering images are acquired with a two-dimensional spectrometer. The images are then unfolded with an experimental machine function.[38]

In the following, this article provides an account of the reaction dynamics experiments on ion–molecule reactions that have been carried out during the last years using the velocity map ion imaging technique. The interpretation of the experimental results always benefits substantially from comparison with high-level dynamics calculations and several references to such calculations will be given. The next section discusses different types of cation–molecule reactions, followed by a description of negative ion–molecule reactions. At the end we give an outlook with our personal view on the future of the field.

Cation-neutral reactions

Cations can be formed by interactions with energetic particles. Thus, their chemistry is important in high energy environments such as the upper planetary atmosphere, regions of the interstellar

medium or technical plasmas. The charge transfer between a cation and a neutral molecule is a prominent reaction channel once it is energetically accessible. It is a conceptually simple reaction just transferring an electron, but it is often a first step that triggers a cascade of further elementary reactions.[39,40] In the case of near resonance between both reactants, the transfer of an electron will happen with minimal momentum transfer. The newly formed ion will move with the same velocity as the neutral precursor. However, resonance phenomena can dominate the dynamics and energetics and lead to a break down of the Born–Oppenheimer approximation. In reactants with a hydrogen bond, the hydrogen atom transfer reaction competes with the charge transfer. Hydrogen transfer reactions take up key positions in molecular networks within the interstellar medium,[41,42] the atmosphere of planets[43] and also biomolecular environments.[44,45] The hydrogen can be transferred as proton H^+, H atom radical or even as a hydride H^- anion. Reactive collisions might also lead to the formation of new bonds with heavier elements, such as carbon or nitrogen. The reactions investigated in the next paragraphs range from resonance effects in atom–diatom charge transfer to bond forming reactions. In many reactions, charge transfer is only the first elementary reaction which is followed by secondary processes such as dissociation. A special case of competing pathways is the formation of isomeric species which will be discussed for the formation of HOC^+/HCO^+.

Resonances in Ar^+ diatom charge transfer reactions

Charge transfer reactions commonly proceed at long range with minimal momentum transfer between both reactants. However, the change in charge state is likely to induce a structural change of the molecule's shape going from the neutral to the ionic species, which affects its vibrational motion.[46,47] Near-resonant channels along the reaction coordinate, which lead to product ions in specific rovibrational states, can result in a break down of the Born–Oppenheimer approximation[48] which makes the accurate theoretical description of the experimental results challenging.

In the reaction of the argon cation Ar^+ with molecules resonant charge transfer channels involving specific vibrational states have been observed.[40,49–51] In the reaction with molecular nitrogen N_2 (reaction (1)),

$$Ar^+(^2P_J) + N_2(^1\Sigma_g^+) \rightarrow Ar(^1S_0) + N_2^+(^2\Sigma_g^+,v') \quad (1)$$

the product ion N_2^+ is predominantly formed in vibrationally excited states although these pathways are slightly endoergic. Vibrational state analysis reveals that most ions are found in the $v' = 1$ vibrational state although only the formation of N_2^+ in $v' = 0$ is exoergic. These results from early crossed beam experiments could be explained by a model employing Landau–Zener curve crossings along the vibrationally adiabatic potential curves.[52,53] A crossing does not exist for the ground state. Furthermore, the model predicts the excitation of higher vibrational states at smaller impact parameters. Crossed beam velocity map imaging experiments[31,54] were able to record angle differential scattering cross sections (see Fig. 1, right column). The forward scattered distribution shows the highest intensity at small angles and

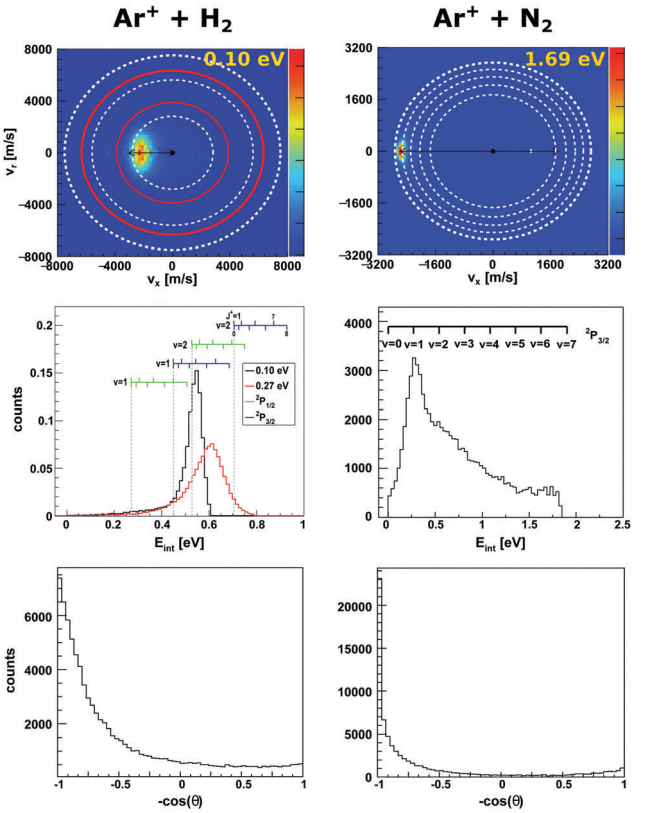

Fig. 1 Experimental reactive scattering results for the charge transfer reactions $Ar^+ + H_2$ (left column) and $Ar^+ + N_2$ (right column). The upper panels show the H_2^+ and N_2^+ product velocity distributions. The right color bars represent a linear ion intensity scale. For $Ar^+ + H_2$, the rings drawn into the velocity distributions give the kinematic limit for $Ar^+(^2P_{1/2})$ (white rings) and $Ar^+(^2P_{3/2})$ (red rings) with the outermost rings for the H_2^+ vibrational ground state and the inner rings for one or two quanta of vibrational excitation. For $Ar^+ + N_2$ the rings give the vibrational levels for the reaction with $Ar^+(^2P_{3/2})$. The middle panels depict the corresponding product internal energy distributions. For the reaction with H_2, a forward cone of 30° was evaluated. The insets visualizes the vibrational and rotational levels of H_2^+. The upward ticks represent reactions with *ortho*-H_2 and downward ticks of *para*-H_2. In case of N_2^+ only vibrational levels are given. The lower panels present the integrated product scattering angle distributions. The data are reproduced from ref. 55 and 54.

peaks at $v' = 1$. However, also scattering into larger angles is present, which can be seen in the angle integrated intensity profile. Smaller impact parameter collisions lead to this larger angle scattering. Analysis of the internal energy distribution as a function of scattering angle reveals a higher vibrational excitation at larger scattering angles in qualitative agreement with the predictions from the Landau–Zener model.

In the reaction of Ar^+ with molecular hydrogen H_2 and its isotope D_2,

$$Ar^+(^2P_J) + H_2/D_2(X,v,J) \rightarrow Ar(^1S_0) + H_2^+/D_2^+(X,v',J') \quad (2)$$

$$\rightarrow ArH^+(X,v',J') + H(^2S_{1/2}) \quad (3)$$

the ratio of charge transfer to hydrogen transfer (reactions (2) and (3)) is strongly dependent on collision energy with both reactions being exothermic.[56] At low collision energy hydrogen

transfer is dominant. The reaction dynamics were initially described by a capture model,[10,57,58] but experiments found that the combined total cross sections of both reaction pathways exceed the Langevin cross section at low collision energies.[56,59] The authors of the experimental studies argue that the first step is an electron jump from H_2 to the argon ion. In a second step, a proton is transferred from H_2^+ to argon. The higher polarizability of the argon atom compared to H_2 brings experiment and capture model into agreement again. Therefore, the charge transfer reaction coordinate is often considered to be a part of the reaction coordinate leading to the hydrogen transfer which, therefore, is often referred to as proton transfer.

In the reaction with N_2 the two spin orbit states of Ar^+ show no difference in reactivity, with the excited state being even slightly less reactive.[60] In the reaction with H_2 the spin orbit excited Ar^+ $^2P_{1/2}$ state is significantly more reactive than the $^2P_{3/2}$ ground state.[59] The H_2^+ is predominantly formed in the second vibrationally excited state ($v' = 2$). This is caused by a quasi resonance in the energetics of entrance and exit channel for $Ar^+(^2P_{1/2}) \rightarrow Ar + H_2^+$ ($v' = 2$). A seam between the potential energy surfaces due to an avoided crossing[61–63] opens an efficient reaction pathway. This resonance can no longer be observed in the reaction with D_2. Additionally, the reactivity for both spin orbit states of Ar^+ in the reaction with D_2 is comparable.

To gain a full understanding of the involved dynamics, recent experiments recorded full angle and energy differential cross sections by crossed beam velocity map imaging for the reaction $Ar^+ + H_2$. In reaction with spin orbit excited argon ions, forward scattering into H_2^+ in $v' = 2$ is the dominant scattering feature in the image[55] (see Fig. 1, left column). The dashed rings indicate the vibrational state of the H_2^+ product ion. The outermost ring corresponds to the vibrational ground state of H_2^+. In the reaction with ground state argon only the first excited vibrational level is energetically accessible given the experimental conditions. The spin–orbit excited level of Ar^+ lies 178 meV above the ground state and this allows also the second vibrational level to be populated. Contrary to prior experiments recording angle differential cross sections,[64] only a minor backward fraction was observed. Analysis of the internal energy distribution revealed significant rotational excitation of the product H_2^+ ions. A maximum of four quanta of rotational excitation can be found at a collision energy of $E_{coll} = 0.1$ eV (see middle row Fig. 1) and up to $8\hbar$ at a collision energy of $E_{coll} = 0.28$ eV.[55] The reactant H_2 beam was generated by supersonic expansion and molecules can be considered to be mostly in the rovibrational ground state at the experimental conditions. Given the single collision conditions in the experiment, more than one rotational quantum has to be transferred into rotational excitation in a single reactive collision. A two step model was proposed to explain the rotational excitation. In a first step, the electron jumps form the H_2 to Ar^+ at long range. This changes the potential from Ar^+–H_2 to Ar–H_2^+, on which rotational inelastic scattering may take place as a second step. In the inelastic collisions angular momentum is transferred into rotational excitation of H_2^+. The energy transfer in these inelastic collisions can be very effective as recently shown for $He + H_2^+$.[65] The same degree of rotational excitation can be found for the backward scattered H_2^+ ions. At these small impact parameter collisions less total angular momentum is available. Thus, the transfer of angular momentum to rotational excitation must be even more efficient than in the atomistic mechanism leading to forward scattering.

Charge transfer and hydrogen transfer in heavy–light heavy reactions

In exothermic charge transfer reactions a significant amount of energy might become available to the reactants. Under single collision conditions in gas phase experiments this energy cannot be dissipated to surrounding solvent molecules but has to be redistributed among the reaction products. Farrar and co-workers investigated the dynamics of charge transfer reactions using crossed beam velocity map imaging experiments at several electron volt collisions energy. The high collision energy combined with the exothermicity of the reaction enables the transfer of a considerable amount of energy into internal degrees of freedom of molecular products. This opens the possibility of dissociative charge transfer, where the primary molecular product fragments due to the high degree of internal excitation.[66] This process often happens on such fast time scales that the dissociation reaction is considered to be a direct dynamical process. Similar to the initial charge transfer product ion, almost no momentum transfer occurs to the fragment ion, and the differential scattering cross section will be similar to that of the parent molecular ion. The charge transfer happens in a stripping-like mechanism leading to forward scattering with little momentum transfer. This situation is encountered in the reaction of $N^+ + CH_4$[67] or for $N^+/O^+ + CH_3OD$.[68] In the reaction of N^+ with methane

$$N^+ + CH_4 \rightarrow N + CH_4^+ \rightarrow N + CH_3^+ + H \quad (4)$$

$$\rightarrow N + CH_2^+ + H_2 \quad (5)$$

the primary highly excited CH_4^+ product ion fragments and CH_3^+ and CH_2^+ ions are formed (reaction (4) and (5)). A central motif in these reactions is the combination of $A^+ + BC$ in the form heavy–light–heavy, with the light constituent being a hydrogen atom.

In many of the systems investigated by Farrar and co-workers, charge transfer is dominant over proton transfer. Through a variation of the charge state ($OH^{+/-} + C_2H_2$)[69,70] or the proton donor ($H_2O^+/H_3O^+ + NH_3$),[71,72] they were able to investigate the proton transfer dynamics. A direct stripping mechanism was found to be the only reaction pathway. Their experiments reveal forward scattering close to the kinematic cut-off with little momentum transfer to the ionic product. The mechanism is dominant in any of the investigated systems. Reaction exothermicties are almost completely transferred into internal degrees of freedom of the reaction product. Whereas even at high collision energies the reactant velocity is conserved within the velocity of the proton transfer product due to the lack of momentum transfer during the reactive collision. This is a signature of a fast stripping mechanism which occurs at large impact parameters. The direct comparison of OH^+ and OH^- in

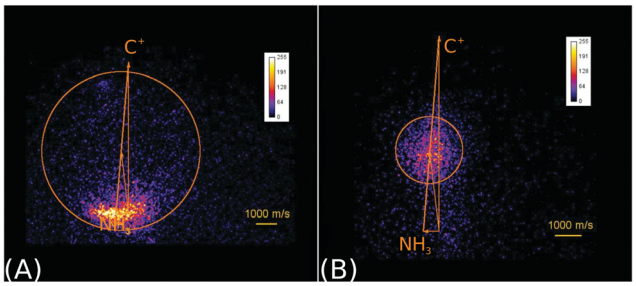

Fig. 2 Raw product ion velocity distributions for the reaction of $C^+ + NH_3$ from crossed beam velocity map imaging experiments at 2.1 eV relative collision energy. Left panel: The charge transfer product NH_3^+ (reaction (6)) is the dominant reaction channel. Right panel: A complex mediated mechanism leads to the formation of a new C–N bond in the product ions $HCNH^+/CNH_2^+$ (reaction (7)). The isomers cannot be assigned. The newton diagrams inset into the scattering images give the relative orientation of the velocity vectors. The circle around the center of mass indicates the maximum product ion velocity considering energy and momentum conservation. Reprinted with permission from ref. 38.

reaction with C_2H_2 reveals similar dynamics for the proton transfer reaction, which occurs for both charge states.

In the reaction of the carbon cation C^+ with ammonia NH_3

$$C^+ + NH_3 \rightarrow NH_3^+ + C \quad (6)$$

$$\rightarrow HCNH^+/CNH_2^+ + H \quad (7)$$

no hydrogen transfer channel was observed.[38,73] The reaction is important in the nitrogen molecular network of the interstellar medium.[73] The charge transfer channel (reaction (6)) is dominant at high collision energies like the investigated energy range in the present study (E_{col} = 1.5–3 eV). Exemplary, raw velocity map images are shown in Fig. 2 at a collision energy of 2.1 eV. The dynamics indicate a stripping like mechanism at large impact parameters for the charge transfer due to minimal deflection of the NH_3^+ ions from the initial NH_3 velocity vector. The authors even speculate if the process might be influenced by resonance phenomena involving the NH_3 umbrella bending vibration[74] because the kinetic energy distribution of the NH_3^+ ions resembles the Franck–Condon profile of the photo electron spectrum.[74,75] The second product ion channel is the formation of a C–N bond which leads to two possible isomers $HCNH^+$ and H_2CN^+ (reaction (7)). The formation of HCN^+ cannot be excluded but was found to be of lower intensity in previous studies.[73,76] The product ion intensity is almost isotropically centered around the center of mass (see Fig. 2B). This refers to the formation of a complex whose lifetime exceeds a rotational period and decays statistically. The reaction is expected to proceed *via* the insertion of the C^+ into an N–H bond followed by the elimination of H or H_2 from the complex. During the complex' lifetime the energy can be effectively redistributed among the internal degrees of freedom.

Isomer specificity in proton transfer reactions: HCO^+/HOC^+ formation

Gas phase proton transfer reactions are thought to be one of the most relevant type of bimolecular interactions influencing the composition of the interstellar medium.[4,77,78] Arguably the most relevant products of interstellar proton transfer processes are the formyl (HCO^+) and isoformyl (HOC^+) isomer cations,[79] which can be formed *via* a variety of reactions, such as:

$$H_3^+ + CO \rightarrow HCO^+ + H_2 + 1.76\ eV$$
$$\rightarrow HOC^+ + H_2 + 0.03\ eV \quad (8)$$

$$HOCO^+ + CO \rightarrow HCO^+ + CO_2 + 0.55\ eV$$
$$\rightarrow HOC^+ + CO_2 - 1.18\ eV \quad (9)$$

There has been a long and still open debate regarding the interstellar HOC^+/HCO^+ branching ratio.[80–82] More specifically, it seems that the ratio does strongly depend on the specific chemical environment of each investigated interstellar region. Reaction (8) forms both the stable HCO^+ or the metastable HOC^+ *via* two exothermic and barrierless channels, with the former being considerably more exothermic. Each pathway proceeds *via* an intermediate ion–dipole complex that follows dissociation to the final products.[83] In contrast to $H_3^+ + CO$, reaction (9) leads to formation of only HCO^+ under thermal conditions, with formation of HOC^+ being endothermic by 1.18 eV. The enthalpy difference between both proton transfer channels in reactions (8) and (9) amounts to 1.73 eV, resembling the difference in proton affinity of the carbon- and oxygen ends of CO.[84] Proton migration between both isomers has been shown to be efficiently catalyzed by neutral molecules such as CO_2 and H_2, which possess a higher proton affinity than the O-side of CO.[85] Moreover, $HCO^+ \leftrightarrow HOC^+$ autoisomerization can occur between highly internally energized product ions, after overcoming a potential barrier of 3.57 eV above the energy of the formyl cation product.[86] The stationary points and main pathways for reaction (8) are schematically depicted in Fig. 3(A).

Given the large difference in reaction enthalpies for the formation of either isomer in both reactions, it should be possible to distinguish between product isomers in a velocity map ion image thanks to energy conservation. This has been the focus of two recent studies on reactions (8) and (9), where we have crossed a beam of H_3^+ or $HOCO^+$ ions at an internal temperature equal to room temperature with a supersonically expanded CO molecular beam at varying collision energies.[87,88]

Fig. 3(B) and (C) depict the center-of-mass product velocity images and associated internal energy distributions for the above-mentioned reactions. The depicted red and white circles denote the kinematic limits for the formation of formyl and isoformyl cations, respectively. These limits represent the maximum center-of-mass speed allowed for the product ions given the collision energy and the respective reaction enthalpy. Thus, in the ideal case of minimal collision energy spread, a product event scattered with velocities larger than the radius of the white circle can solely be ascribed to the HCO^+ isomer. Forward scattering in the direction of the initial CO, as well as a high degree of product internal excitation, are obtained for both reactions at all relative collision energies. Most importantly, a monomodal velocity distribution is observed, preventing a direct estimation of isomer ratios. While the major fraction of product events fall inside both kinematical limits in $H_3^+ + CO$ due to

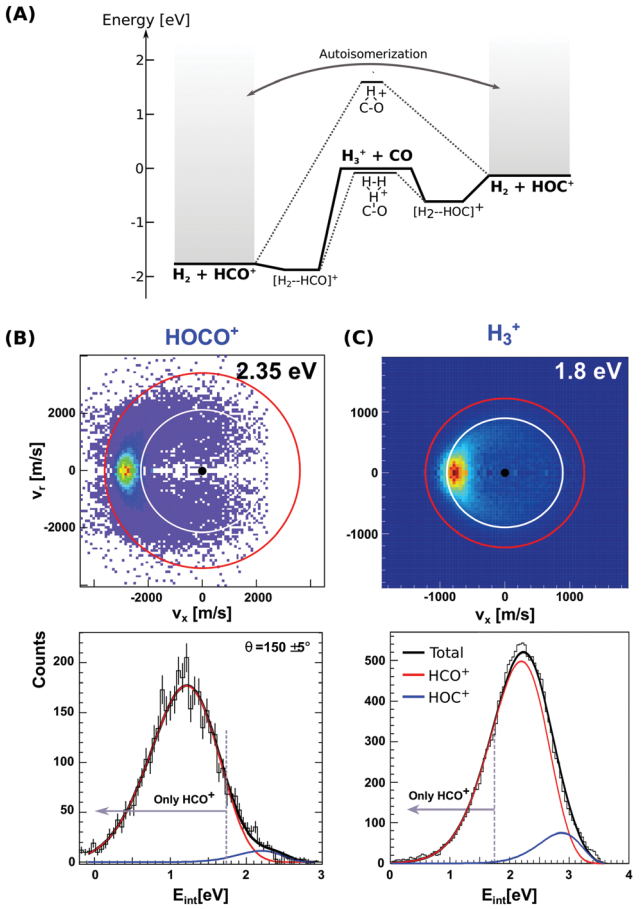

Fig. 3 (A) Calculated minimum energy paths for the reactions H_3^+ + CO (from ref. 83). The energetics for H_2-catalyzed isomerization and auto-isomerization between internally hot HCO^+/HOC^+ cations are indicated. (B and C) Center-of-mass velocity distributions of product HCO^+/HOC^+ ions from reactions H_3^+ + CO and $HOCO^+$ + CO. The red and white rings mark the kinematic limits for formation of HCO^+ and HOC^+, respectively. Lower panels: Corresponding product internal energy distributions fitted to a sum of Gaussians resembling the contribution of HCO^+ and HOC^+ products. Events falling left from the grey bar at 1.73 eV can only correspond to HCO^+ ions. The data are reproduced from ref. 87 and 88.

high product internal excitation, $HOCO^+$ + CO presents a different situation, with almost all reactive events are scattered with velocities larger than the given kinematic limit for HOC^+ formation (see Fig. 3B).

In order to extract the product isomer ratio, the corresponding internal energy distributions are fitted using a sum of two Gaussian distribution functions, as shown in the lower left panel of Fig. 3. An upper limit of 24% HOC^+ is obtained at a scattering energy of 1.8 eV, whereas the value decreases to less than 10% for the two smaller collision energies of 0.2 and 0.6 eV. For $HOCO^+$ + CO, a maximum contribution of (1.5 ± 0.2)% for HOC^+ is obtained, making this system an HCO^+-specific product forming reaction even at relative collision energies above the threshold for HOC^+ formation.

From a statistical perspective, the higher density of rovibrational states for the HCO^+ geometry than for the HOC^+ geometry is supposed to favor the transfer of the proton to the carbon end of CO. In addition, possible reorientation effects in CO towards a H–C interaction may play a role. The possibility of H_2/CO_2-catalyzed isomerization from HOC^+ to HCO^+ is predicted to be a slow process if compared to fast proton exchange and is thus not expected to affect the isomer branching ratio. This is supported by the lack of low velocity products ions that would most likely result from such a rearrangement.

Competing formation channels in O^+ + CH_3Y reactions

The oxygen cation O^+ is an important constituent of the atmospheric chemical network. Methyl halide molecules of anthropogenic origin can be found in the atmosphere.[89,90] Pei *et al.* studied the reaction

$$O^+(^4S) + CH_3Y \rightarrow CH_3Y^+ + O \quad (10)$$

$$\rightarrow Y^+ + CH_3 + O \quad (11)$$

$$\rightarrow CH_3^+ + YO \quad (12)$$

for a series of methyl halides CH_3Y with Y = Br, Cl, I[91] using velocity map imaging. Three main product ion channels were identified: CH_3Y^+ (reaction (10)), Y^+ (reaction (11)) and CH_3^+ (reaction (12)). Reactions (10)–(12) are all exothermic for all three investigated halide species with the exception of Br^+ formation. The first two are formed by charge transfer and subsequent dissociation. These channels had been seen previously in selected ion flow tube experiments.[92] The velocity map images for all product channels for the reaction of CH_3I + O^+ are shown in Fig. 4. The charge transfer leads to the typical narrow distribution peaking at the velocity of the precursor molecule due to the little momentum transfer during the reaction (see Fig. 4(A)). The distribution of the I^+ ions is slightly broader than for the charge transfer product CH_3I^+ but still corresponds to a fast dissociation allowing the analysis of the product energy distribution.[93–95]

The most abundant reaction product is the methyl cation CH_3^+. The distribution is centered isotropically around the center of mass at far lower velocities compared to the product ions from the other two reaction pathways, which are centered at the neutral beam velocity (see Fig. 4). Analysis of the kinetic energy distribution reveals two contributions to the differential cross section. The first, a peak at almost zero kinetic energy, shows strong forward scattering, while the second contribution is a high energy tail that extends to almost 3 eV kinetic energy. This tail contains almost 75% of the ion flux and shows no angular dependence. These findings indicate two independent atomistic reaction pathways. The forward scattering pathway results from a cleavage of the carbon–halogen bond on the initial spin surface.[92] Along the second pathway, in a first step a CH_3OY^+ complex is formed which lives longer than at least one rotational period leading to the observed isotropic scattering.[97] The CH_3^+ formation from the CH_3OY^+ complex is spin forbidden on the initial ground state doublet surface of the intermediate complex. After complex formation, the reaction coordinate has to cross to the quartet surface to proceed to the CH_3^+ formation. This process is mediated by spin–orbit coupling and thus explains the different behavior seen for the three investigated methyl halides. The branching ratio, as well as the contribution of the complex mediated pathway to the CH_3^+ formation, is

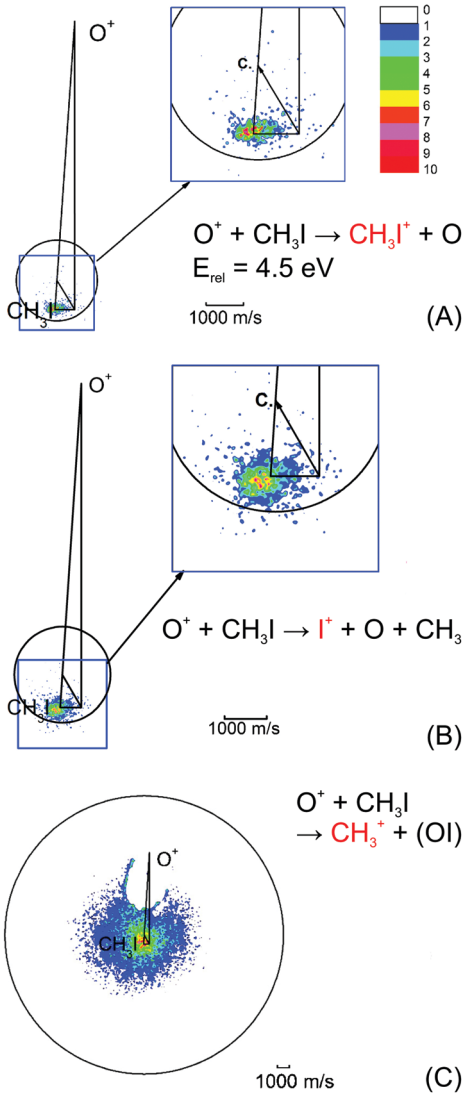

Fig. 4 Velocity map images for all three possible product channels in the reaction $CH_3I + O^+$: (A) CH_3I^+, (B) I^+ and (C) CH_3^+. The formation of CH_3^+ is the dominant product channel in the reaction with CH_3I (65%). The charge transfer product CH_3I^+ is the least abundant (15%). The circle indicates the maximum ion velocity considering energy and momentum conservation. Reprinted with permission from ref. 96.

strongly dependent on the halide ion. The contribution of the CH_3^+ channel is highest for methyl iodine.

Metal ion–hydrocarbon reactions

The reactivity of hydrocarbons in reactions with transition metal ions has already been investigated for several decades.[98–100] The group of James Weisshaar extended their experiments with crossed beams[101–105] to investigate the reaction of the cobalt cation with small saturated hydrocarbon molecules using velocity map imaging:[30,106]

$$Co^+(^3F_4) + nC_3H_8 \rightarrow CoC_3H_8^+ \quad (13)$$

$$\rightarrow CoC_2H_4^+ + CH_4 \quad (14)$$

$$\rightarrow CoC_3H_6^+ + H_2 \quad (15)$$

In the reaction $Co^+ + C_3H_8$ they found three major product channels (reactions (13)–(15)).[106,107] In their experiment, the electronic state of the cobalt cation was controlled by selectively forming the ground state $^3F_4$ of the ion by photoionization.[108] The product ions are scattered almost isotropically at low velocities around the center of mass for all three product channels. The dominant channels are the formation of the $CoC_3H_8^+$ complex (reaction (13)) and the elimination of molecular hydrogen from the initial encounter complex (reaction (15)). Only about 15% of the reaction leads to methane elimination (reaction (14)). The total cross section is estimated to be less than 10% of the Langevin cross section.[58] The methane elimination shows a statistical energy distribution for the product molecules whereas the hydrogen formation shows a non-statistical behavior in agreement with previous studies by Bowers and co-workers.[109–111] The results can be explained by the formation of a multi center transition state (MCTS) by either insertion of the Co^+ in the C–C bond leading to methane elimination or into a secondary C–H bond leading to H_2 formation. The formation of the MCTS is a concerted step and represents the rate limiting step along the reaction coordinate. In both cases a β-H shift leads to product formation. The resulting exit channel complexes $(H_2)Co^+$ (C_3H_6) and $(CH_4)Co^+$ (C_2H_4) are trapped in the potential well of the exit channel. However, the heavy Co atom effectively decouples the H_2 from the formed propylene and thus prevents internal vibrational relaxation. The H_2 can escape the potential well and form the fast products whereas the methane is efficiently thermalized within the well.

Weisshaar and co-workers tested the general concept derived for the reaction with propane (reactions (13)–(15)) by replacing a hydrogen atom by a methyl group and investigated the reaction of Co^+ with iso-butane:[30]

$$Co^+(^3F_4) + \text{iso } C_4H_{10} \rightarrow CoC_4H_{10}^+ \quad (16)$$

$$\rightarrow CoC_3H_6^+ + CH_4 \quad (17)$$

$$\rightarrow CoC_4H_8^+ + H_2 \quad (18)$$

Here, the signal for the CH_4 formation pathway is five times more intense than that for H_2 elimination. The translational energy distribution for the H_2 pathway shows the high energy tail already seen in the reaction with propane (see Fig. 5). Data from the Bowers group is given as comparison.[112,113] Both experiments observe a hot non-statistical tail in the distribution for H_2 products while the CH_4 products follow a statistical decay.[114] The authors claim that no late barrier in the exit channel is responsible for the non-statistical behavior. The reaction coordinate rather moves through a multi center transition state to an exit channel complex. Structures for the multi center transition states are given in insets of Fig. 5. This reaction coordinate follows the same minimum energy path as the reaction with propane. The only exception is the preferred insertion of the Co^+ into the tertiary C–H bond compared to the secondary C–H bond in propane. Employing the MCTS-model the reaction can proceed on a single spin surface. Further support for the model is gained by experiments with deuterated alkanes leading to HD or D_2 elimination.[110–113] The kinetic isotope effect experiments lead to a "colder" translational energy distribution.

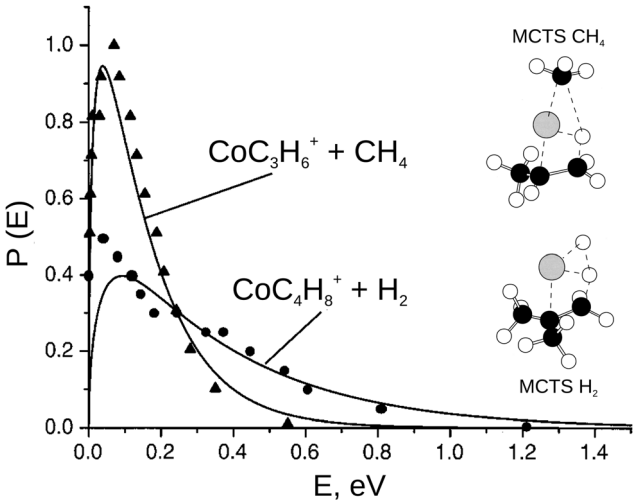

Fig. 5 The product translational energy distribution $P(E)$ for the CH_4 elimination and the H_2 elimination channel in the reaction Co^+ + iso-C_4H_{10} (solid lines) in comparison with prior work from the Bowers group (triangles = CH_4 products and circles = H_2 products, data from ref. 113). Only about 10% of the available energy is partitioned into product translation in CH_4 channel compared to 35% for the H_2 channel. The H_2 shows a non-statistical high energy tail. The insets show the geometry of the multi center transition states for both reaction pathways. Reprinted with permission from ref. 30.

This is not to be expected for a stepwise mechanism. However, it is conceivable that the heavier mass of HD or D_2 slows down the escape from the reaction complex. The longer time spent in the exit well leads to an equilibration and thus a colder product ion ensemble. The results for propane and iso-butane are in agreement and can be explained by a single concept for the reaction coordinate. This model is able to explain the experimental findings in a general framework and can possibly also be applied to reactions with Ni^+ and Fe^+.

Cation-radical reactions

The reactivity of radicals is of great importance in many environments, *e.g.* the atmosphere and the interstellar medium. Radicals are highly reactive and are often formed as intermediate species. The reaction of H_3^+ with the methyl radical CH_3

$$H_3^+ + CH_3 \rightarrow CH_3^+ + H_2 + H \quad (19)$$

$$\rightarrow CH_4^+ + H_2 \quad (20)$$

was investigated by Farrar and co-workers by a combination of crossed beams with velocity map imaging.[115] The dominant reaction channel is charge transfer forming the CH_3^+ cation (reaction (19)). Due to the presence of only a single electron in CH_3 to accept a proton, the proton transfer reaction forming CH_4^+ (reaction (20)) is very inefficient. This endothermic process only opens at higher collision energies. An alternative way to promote the reaction is the vibrational excitation of the H_3^+ reactant ion which was shown to be essential in the experiments by Pei *et al.* to promote the reaction. The H_3^+ was produced by electron impact and thus was vibrationally excited by at least 1 eV. Like in previously studied systems the reaction proceeds *via* a stripping like mechanism at large impact parameters

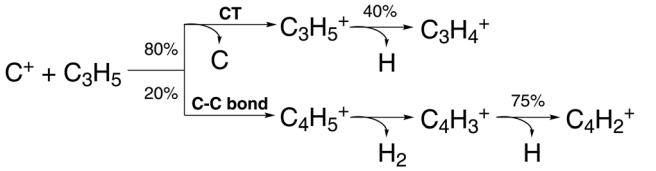

Fig. 6 Scheme of reaction pathways for the reaction $C^+ + C_3H_5$ forming the product species observed by Pei *et al.*[91] The percentage numbers indicate the obtained branching fractions for following the different steps along the reaction pathway.

which results in forward scattering with little momentum transfer to the final product ions CH_3^+ and CH_4^+.

The formation of new C–C bonds is of central importance in synthetic chemistry. The use of carbon based radicals is one possible pathway. Pei *et al.* investigated the reaction of C^+ in reaction with the allyl radical C_3H_5:[91]

$$C^+ + C_3H_5 \rightarrow C_3H_5^+ + C \quad (21)$$

$$\rightarrow C_4H_5^+ \quad (22)$$

They chose a collision energy of 2.2 eV. The primary elementary reaction is highly exothermic, thus depositing several electron volt within the internal degrees of freedom of the product ions (see Fig. 6). The dominant product channel is the charge transfer which proceeds at long range with minimal momentum transfer from the molecular precursor to the product ion (reaction (21)). Dissociation of almost half of the charge transfer products to $C_3H_4^+$ + H is observed.[95] The formation of the new C–C bonds leads to cyclic molecules which is inferred from a theoretical model.[91] Isotropic scattering at small velocities around the center of mass was measured for the ionic products from this pathway. In a first step a complex $C_4H_5^+$ of both reactants is assumed to be formed, which lives at least one rotational period and leads to the observed differential scattering cross section. The internally highly excited product ions further stabilize by the formation and elimination of molecular hydrogen.[116] In a third step, a hydrogen atom might be ejected from the $C_4H_3^+$ intermediate (see Fig. 6). However, the measured image did not allow to make a distinction between a possible open chain or cyclic hydrocarbon molecule.

Anion-neutral reactions

Most natural elements and many molecules are known to efficiently form stable anions. Their stability is directly correlated with the electron affinity of the respective neutral counterpart. As anions often bind their outer electrons rather weakly, they play an important role for the ion-neutral chemistry in environments where they are formed. In low density regimes such as planetary atmospheres or the interstellar medium, formation of anions commonly proceeds *via* radiative association. Several anions have been identified in various astronomical environments,[117,118] and the understanding of their formation mechanisms is an ongoing field of research.[119,120] In solution, anion-induced reactions are common in the formation or cleavage of bonds.

Among the large number of organic reactions where ionic intermediates play a deciding role, bimolecular nucleophilic substitution (S_N2) and base-induced elimination (E2) reactions are perhaps the two most common processes in synthetic pathways leading to carbon bond formation or functional group displacements.[121] In both reactions, bond formation and bond cleavage occur in a concerted way and under stereospecific conditions, which makes these pathways crucial steps for the production of stereochemically pure compounds. Studying the mechanism of such model organic reactions in solvent-free conditions is fundamental to understanding and controlling organic and biomolecular processes. In addition, investigations on micro-solvated reactions provide a precise way of determining the effect of solvent interactions on the reaction on a molecular level.

Elementary nucleophilic substitution reactions

S_N2 reactions have been extensively studied, both experimentally and theoretically, for more than a century.[122–130] The simplest case of an S_N2 reaction corresponds to the attack of a monatomic nucleophile on an alkyl halide,

$$X^- + CH_3Y \rightarrow [X\text{–}CH_3\text{–}Y]^- \rightarrow Y^- + CH_3X. \quad (23)$$

Such model systems can be used to benchmark the main atomistic reaction mechanisms in S_N2 reactions. Textbooks commonly present the typical mechanism of S_N2 reactions to follow three basic steps in a collinear geometry: attack of the nucleophile, formation of a transition state with inversion of the CH_3 moiety and exit of the leaving group. The observed similarities between reaction mechanisms in the gas phase and in solution[131,132] makes studies on isolated reactions appropriate for unraveling intrinsic properties of such processes at single collision conditions. The gas phase S_N2 energy landscape of these type of systems (see Fig. 7, black curve) presents two ion–dipole minima arising from long-range attractive ion–dipole interactions, which are separated by a potential energy barrier caused by repulsive electronic interactions.[133] During the crossing of the barrier, geometrical reorientation of the hydrogen atoms, known as the Walden inversion,[122] takes place in a concerted fashion. The inversion of configuration caused through this mechanism is often used in synthetic chemistry to selectively form specific isomeric compounds.

Despite often being submerged with respect to reactants, it has been shown that this barrier can have a significant effect on the overall reaction kinetics.[134] In particular, it has been demonstrated that $X^- + CH_3Y$ type systems do not behave statistically with respect to energy redistribution at the transition state, but are rather driven by efficient coupling of specific rovibrational modes to the reaction coordinate.[124,135–138] The reaction probability depends on the interplay between complex lifetime and redistribution of energy between inter- and intramolecular degrees of freedom.

The collinear geometry (C_{3v}) in S_N2 reactions is favored by an efficient overlap of the highest occupied molecular orbital (HOMO) of the nucleophile's lone pair with the backside lobe of the lowest unoccupied σ^* molecular orbital (LUMO) of C–Y in the neutral reactant.[139] The sideways interaction is hindered by steric crowding and inefficient molecular orbital overlap.[140] While this approach symmetry has been assumed as being the only valid picture of an S_N2 reaction for decades, initial theoretical investigations already suggested the presence of alternative approach geometries.[141,142]

Gas phase reactive scattering experiments performed in our laboratory using the crossed beam velocity map imaging technique have provided direct evidence for a large variety of reaction mechanisms in a set of $X^- + CH_3Y$ reactions:

$$Cl^- + CH_3I \rightarrow I^- + CH_3I + 0.55\ eV \quad (24)$$

$$CN^- + CH_3I \rightarrow I^- + CH_3CN + 1.98\ eV \quad (25)$$

$$\rightarrow I^- + CH_3NC + 1.05\ eV$$

$$F^- + CH_3Cl \rightarrow Cl^- + CH_3F + 1.35\ eV \quad (26)$$

$$F^- + CH_3I \rightarrow I^- + CH_3F + 1.84\ eV \quad (27)$$

$$OH^- + CH_3I \rightarrow I^- + CH_3OH + 2.8\ eV \quad (28)$$

Our studies have shown that the S_N2 mechanistic preferences are strongly affected by a variety of factors such as the particular nucleophile, the leaving group, the surrounding solvent or steric substitution.[34,143–146] To shed light into the detailed motion of the atoms leading to the observed product scattering images, close collaborations with chemical dynamics theory is essential. In chemical dynamics simulations, the motion and interaction between the involved atoms are followed using quasi-classical trajectory simulations, either "on the fly" by Hase and co-workers[125,147] or on analytical multidimensional potential energy surfaces that represent the potential energy as a function of relative coordinates of the reactive system by Czakó and co-workers.[148,149] Over the last decade, the collaboration between experiment and theory has led to the identification of many atomic level mechanisms,[150,151] with the most common being:

- A direct rebound mechanism corresponding to the textbook collinear rebound reaction, with the leaving ion being scattered in backward direction with respect to its original motion.

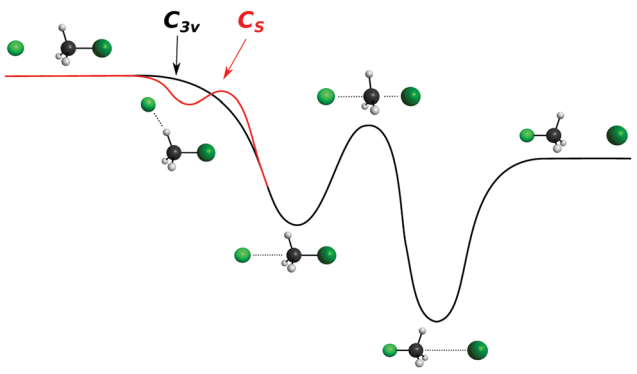

Fig. 7 Schematic representation of a typical minimal energy path for the collinear (C_{3v}) and X–H bonded (C_s) nucleophilic substitution reaction. The optimized chemical structures shown for the most important stationary points have been taken from ref. 143.

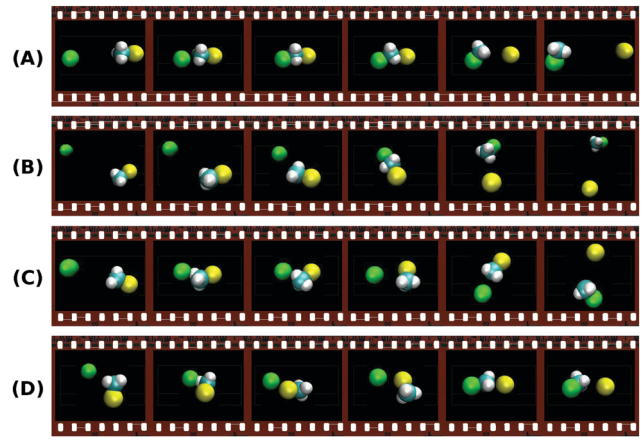

Fig. 8 Exemplary trajectories along the reaction coordinate of a typical S_N2 reaction showing some of the major atomistic mechanisms found in the theoretical simulations:[144,153] (A) direct backward; (B) forward stripping; (C) indirect; (D) roundabout. The full animations of the trajectories can be found at http://hase-group.ttu.edu/animations.html.

• A stripping process where X^- approaches the neutral molecule from the side and strips off the CH_3 moiety, leading to a forward scattered Y^- ion.

• The formation of a transition state complex with a lifetime longer than its rotational period, which leads to a slow Y^- that is isotropically scattered over all angles. The formation of this stable complex has been found to occur *via* both collinear and X–H bonded pre-reaction complexes.[152]

Additional mechanisms such as the roundabout, frontside attack or double inversion pathways have been also reported for some reactions[141,144,151] and are a further indication of the mechanistic richness in S_N2 processes. Fig. 8 shows typical simulated trajectories for the most relevant reaction mechanisms.

Fig. 9 presents the experimental product velocity distributions for reactions (24)–(28) at low (0.4 eV) and high (1.9 eV) relative collision energy.

Electronic structure and direct dynamics simulations can be used to interpret the mechanistic patterns from Fig. 9. The reactions $Cl^- + CH_3I$, $CN^- + CH_3I$ and $F^- + CH_3Cl$ show dominant isotropic scattering at low relative collision energy and a contribution of direct backward scattering. Isotropic scattering has been ascribed to an indirect mechanism associated with efficient translational to rotational energy transfer *via* coupling of the reactant orbital angular momentum and the CH_3Y rotational angular momentum.[135] The direct rebound mechanism is the major pathway at high collision energies and has been found to be particularly efficient at small impact parameters.[150] While these direct reactions are probable only at small X–C–Y angles around the direct backside attack, collisions tend to occur at larger angles due to the insufficient time for reactant pre-orientation,[154] which explains the decrease of the reaction rate coefficient with relative collision energy

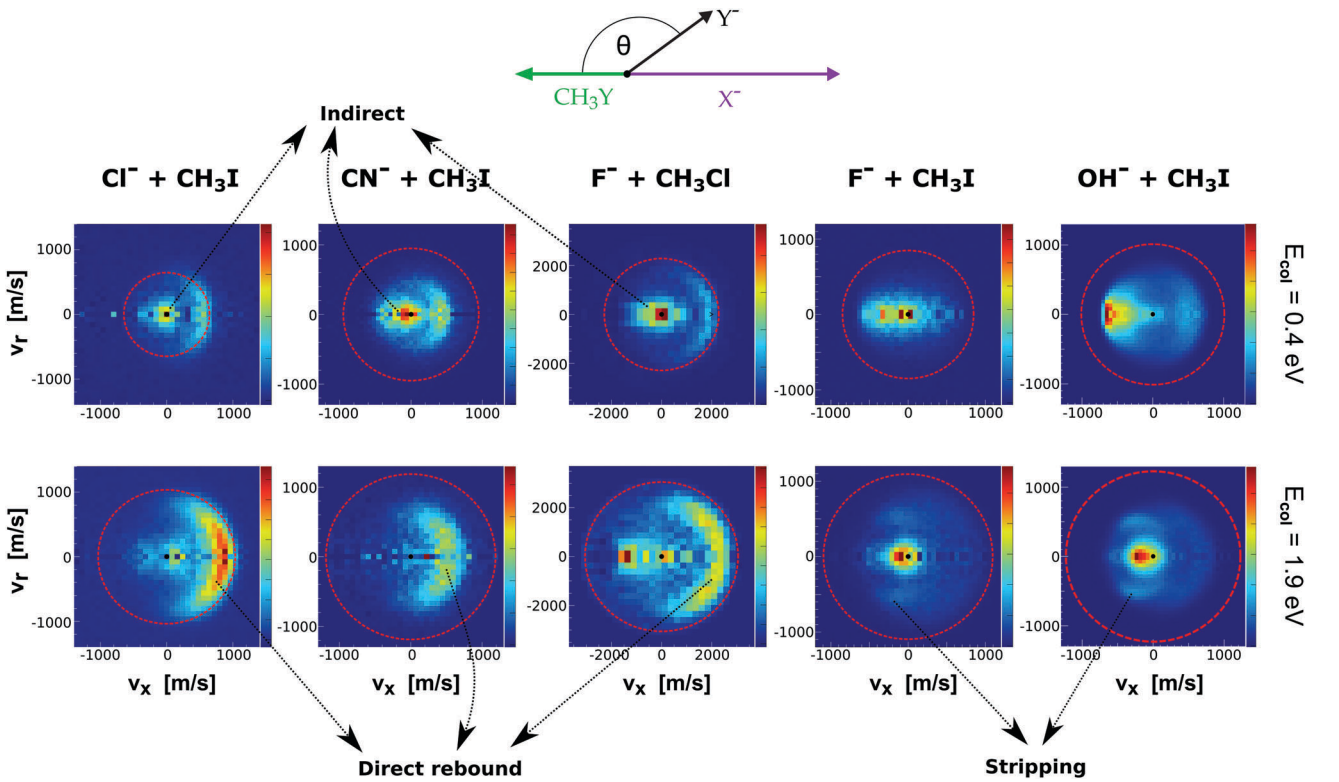

Fig. 9 Center-of-mass velocity distributions of product Y^- ions for five different S_N2 reactions: $Cl^- + CH_3I$,[144] $CN^- + CH_3I$,[146] $F^- + CH_3Cl$,[143] $F^- + CH_3I$,[34] $OH^- + CH_3I$.[145] The data are reproduced from the respective references. The right color bars represent a linear ion intensity scale. Typical scattering patterns ascribed to the direct rebound, stripping, and indirect mechanisms are indicated.

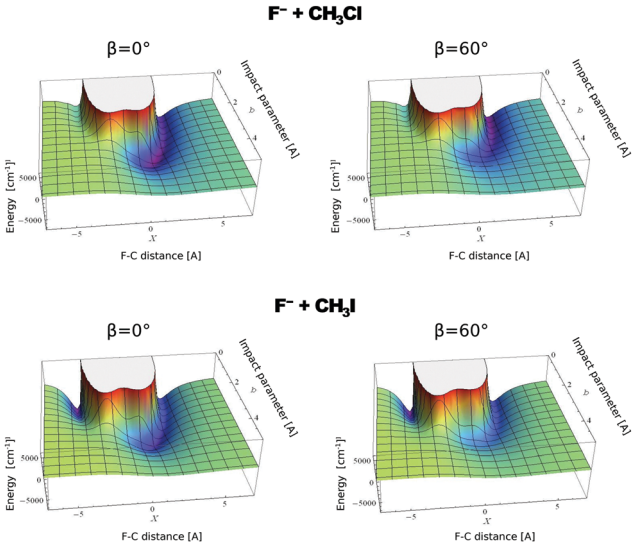

Fig. 10 Computed potential energy for F^- approaching CH_3Cl (up) and CH_3I (low) as a function of impact parameter (b) and F–C distance. The two values of β represent the two possible dihedral angles between the C, Y, H and X atoms. The potentials are reproduced with permission from ref. 159.

observed for several $X^- + CH_3Y$ systems.[142,155,156] In general, the computational analysis renders product ion scattering angle and energy distributions that agree very well with the experimental findings.[143,144,153]

In contrast to the previous results, the product velocity distributions from $F^- + CH_3I$ and $OH^- + CH_3I$ are markedly different, with isotropic and forward scattering at low collision energies and the indirect and stripping mechanisms dominating the reaction dynamics at high relative collision energies.[34,145] This substantial change in the dynamics has been traced back to several factors. Most significantly, it has been demonstrated that both F^- and OH^- strongly favor a non-collinear, X–H bonded pre-reaction complex formation (see Fig. 7), a feature consistent with the high proton affinity of these anions.[152,157,158] In contrast to the above described dynamics, the reaction between F^- and CH_3Cl shows a strong preference for direct rebound dynamics, albeit F^- being the attacking anion.[143] While the calculated *ab initio* potential energy surface of $F^- + CH_3Cl$ also shows the presence of a F–H bonded pre-reaction complex, clear differences in the energy of the dihalide interaction were found. As shown in Fig. 10, a deep energy minimum is obtained for the geometry associated to an F–I interaction in $F^- + CH_3I$, while the interaction is weaker by about a factor of ten for the F–Cl interaction in $F^- + CH_3Cl$.[159]

Proton transfer and dihalide formation

Reactions of negative ions with methyl halides not only lead to nucleophilic displacements, but also promote the formation of alternative reaction products. This is the case of the proton transfer and halogen abstraction channels. These reactions have shown to compete with S_N2 under excess energy conditions in reactions involving F^- and OH^-, in particular $F^- + CH_3I$ and $OH^- + CH_3I$.[160–162] For the former reaction, the formation of CH_2I^- (proton transfer) and IF^- (dihalide formation) are endothermic by 0.6 ± 0.1 eV and 0.7 ± 0.3 eV, respectively. The latter reaction is exothermic and it was found that for temperatures as low as 200 K the proton transfer and the S_N2 reaction have nearly equal reaction probability.[163]

The proton transfer and halogen abstraction channels have only recently started to receive theoretical attention.[157,163–165] For example, it has been shown for $F^- + CH_3I$ that the proton transfer channel features the same X–H bonded pre-reaction complex (C_s minimum in Fig. 7) found for the nucleophilic substitution channel. In a recent experimental work, we have investigated the branching ratio and reaction dynamics of these pathways in $F^- + CH_3I$ as a function of relative collision energy.[166] Formation of a protonated dihalide anion $[FHI]^-$ was identified for the first time during this study. While the S_N2 channel is the dominant product at all studied relative collision energies, all other channels contribute to a considerable extent at energies above 1 eV. In particular, the proton abstraction induced CH_2I^- fragment reaches a maximum branching ratio of 0.2. At energies above 2.6 eV IF^- becomes the second major channel, related to the possible occurrence of C–I bond dissociation at these energies. $[FHI]^-$ appears only above 1 eV relative collision energy, consistent with a calculated reaction enthalpy of 0.9 ± 0.2 eV, and remains a minor channel throughout the studied energy range.

Fig. 11 depicts the center-of-mass velocity distributions of all ions produced in $F^- + CH_3I$ at 2.3 eV (up), as well as the corresponding internal energy distributions (bottom). Both dihalide formations and the proton abstraction reaction present a substantial degree of energy partitioning to product internal degrees of freedom. The fraction of total internal excitation in the proton abstraction channel ranges from 0.55 to 0.35 and decreases with increasing collision energy. The values are in good agreement with a recent theoretical prediction at 1.55 eV[164] and are found to be comparable to the degree of excitation observed in $OH^- + CH_3I$.[157] Compared to the CH_2I^- channel, formation of both dihalide species is found to occur under significantly stronger energy partitioning to internal degrees of freedom. In summary, this work shows that alternative product formation channels compete with S_N2 under excess energy conditions in reactions where non-traditional reactant approach geometries are favored.

Effects of micro-solvation on the dynamics of nucleophilic substitution reactions

Reaction dynamics in the liquid phase are driven by the interplay between the intrinsic reaction dynamics due to the reactants and the interactions induced by solvent molecules.[167] Therefore, the role of individual solvent molecules is of great interest. Studies on bimolecular reactions in solution on the picosecond timescale have revealed a lot of information.[20] Further, it was found that characteristics of the gas phase dynamics persist in solution.[131] Solvent molecules affect the energetics along the reaction coordinate by either stabilizing selected intermediates and transition states or destabilizing them. Hence, kinetics, dynamics, and product branching ratios of a reaction are influenced by the solvent interaction.

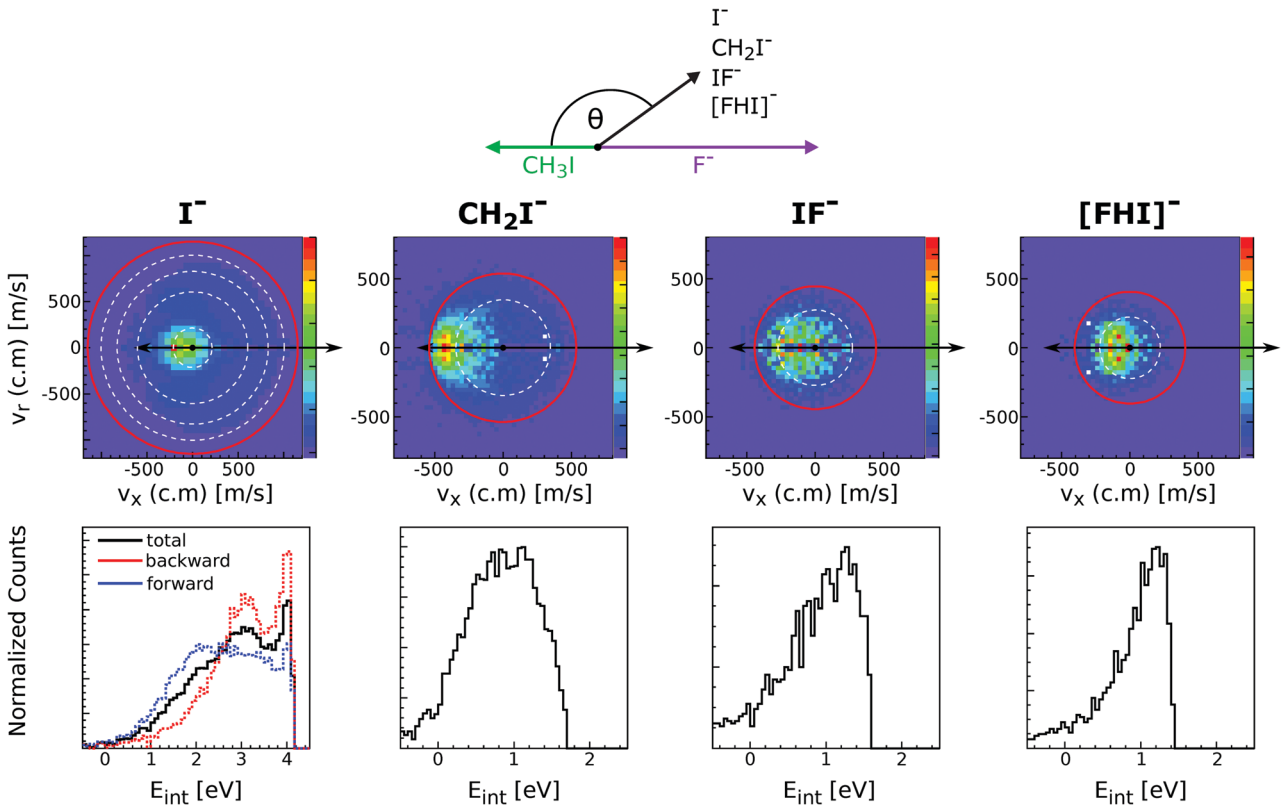

Fig. 11 Experimental scattering results for the different reaction channels in F^- + CH_3I at a relative collision energy of 2.3 eV. The upper panels show the velocity distributions of product I^-, CH_2I^-, IF^- and $[FHI]^-$ ions. The lower panels depict the internal energy distributions associated to each of the product formations. The data are reproduced from ref. 166.

To bridge the gap between gas and liquid phase, experiments using "micro-solvation" are employed. In these experiments, a selected number of solvent molecules is added to one or more reactants. Mass spectrometry allows control of the degree of solvation by accurately determining the mass of the solvated reactant,[168] thereby counting the number of attached solvent molecules. In nucleophilic substitution a polar solvent is commonly used, which motivated investigations with water–nucleophile complexes. One of the studied nucleophiles is the hydroxyl anion OH^-. Rate constants and product branching ratios have been determined at different temperatures (200 to 500 K) for $OH^-(H_2O)_{0-4}$ and $OD^-(D_2O)_{0-2}$ reacting with CH_3Cl or CH_3Br.[169–173] The solvent leads to a suppression of the reaction rate coefficient.[174] As main product channel the formation of the free or only partially solvated ionic product was found, even though the fully solvated ionic product is thermodynamically favored. This non-statistical behavior means that the reaction pathway is strongly influenced by the dynamics. Also numerous theoretical studies investigated the effects of micro-solvation of the nucleophile.[175–182] Several studies showed that the presence of water molecules attached to the nucleophile reduces its reactivity in S_N2 reactions[174,177] as seen by experiments. Further insight was gained by investigating the effect of micro-solvation on individual intermediates.[183–185]

Insights into the effects micro-solvation has on the dynamics has been gained from crossed beam velocity map imaging experiments. The nucleophilic substitution reaction of $OH^-(H_2O)_n$ + CH_3I with n = 0–2 has been investigated.[186] The differential scattering cross sections for the formation of the non-solvated I^- significantly change with the degree of solvation (see Fig. 12). Whereas the free OH^- in reaction with CH_3I shows predominant forward scattering (see Fig. 9), forward scattering can no longer be seen upon micro-solvation. At lower collision energies, once one water molecule is attached to the OH^-, the scattering distribution becomes isotropic around the center of mass at low product ion velocity. This is common for a complex mediated atomistic reaction pathway. At the higher collision energy, the direct rebound opens and competes with the indirect mechanism. In the course of the direct rebound a co-linear arrangement of the O-atom of the attacking OH^- with the C–I bond has to be established. It was found that the interaction of the water molecule with a hydrogen atom of the methyl group steers the OH^- into place. The evolution of the trajectories for both mechanisms are given in Fig. 13. For $OH^-(H_2O)_2$, indirect dynamics are observed at both collision energies. The formation of these low velocity products is assumed to be associated with the formation of a long lived complex which lifetime exceeds at least one rotational period.[186] Direct chemical dynamics simulations support these findings and provide a wealth of additional information on the different reaction mechanisms underlying the observed differential scattering.[187,188]

In the crossed beam experiments, the unsolvated product ion is found to be the dominant product ion. Specifically, the

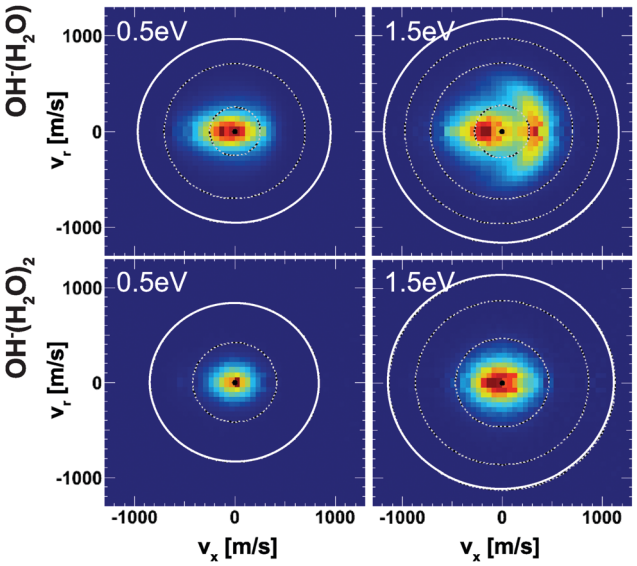

Fig. 12 Velocity map images of I^- product ions from the reaction of $OH^-(H_2O)_{1,2}$ with CH_3I at two collision energies. The outermost ring indicates the kinematic cut-off and the inner rings isospheres of 1 eV translational energy. The data are reproduced from ref. 186.

ratio between I^- and the singly solvated $I^-(H_2O)$ has been determined for reactions of $OH^-(H_2O)$ + CH_3I[189] showing no dependence on collision energy for the low-energy complex mediated mechanism. The abundance of the thermodynamically favored solvated product was found to be less than 5%. This branching ratio has been confirmed by trajectory simulations.[187,190,191] The water molecule leaves before crossing over the barrier forming the product ion (see Fig. 13). In case of the indirect mechanism the water molecule leaves at the same moment the bond rearrangement takes place. At higher collision energies that lead to direct rebound, the water molecule leaves upon impact and the reaction proceeds along the OH^-–CH_3I reaction coordinate. In both cases, the reaction coordinate bypasses the solvated transition state and the dissociation of the micro-solvated complex is either concerted with the bond breaking and formation or even prior to it.

The proton transfer reaction forming the CH_2I^- is accessible at room temperature and constitutes a competing product channel to nucleophilic substitution. For the bare OH^- the proton transfer accounts for almost a third of the product ions already at 0.5 eV.[32] The proton transfer also appears in the micro-solvated case. Here, a remarkable agreement between theory and experiments could be achieved.[188]

A trade-off between energetic and steric effects in the reaction of micro-solvated flouride ions F^- with methyl iodide has been found in theoretical studies. Investigations of singly solvated $F^-(H_2O)$[174,181,192] have been extended up to three attached water molecules, $F^-(H_2O)_{0-3}$.[173] It was found that the reaction coordinate does not cross the barrier of the fully solvated transition state complex. Subsequent loss of one or two water molecules occurs and the barrier is crossed at the $F^-(H_2O)$ level. This leads again to favoring the thermodynamically less stable product which is the free I^- like for micro-solvated OH^-.

Base induced elimination

A very interesting example for the competition of two different reactions is the competition between nucleophilic substitution (S_N2) and base-induced elimination (E2), both important reactions in organic chemistry. X^- + CH_3Y type reactions can only produce the fragment Y^- *via* S_N2, irrespective of the specific mechanism involved. However, if the hydrogen atoms in CH_3Y are replaced by one or more methyl groups, the base-induced elimination (E2) reaction starts to play an important role. The extreme case of CH_3 addition to CH_3Y is represented by a *tert*-butyl halide, $(CH_3)_3CY$, where the anion can attack one out of nine equivalent hydrogen atoms. In addition, the bulky CH_3 groups will strongly hinder a potential nucleophilic attack to the central carbon. Both S_N2 and E2 share several similarities: they are concerted processes and produce exactly the same product ion. Due to the fact that strong nucleophiles are usually also strong bases these two processes are in intrinsic competition with each other. Fig. 14 illustrates the textbook transition state structures and products for both S_N2 and E2. As depicted in this figure, an α-C denotes the carbon atom attached to a functional group, *e.g.* the halogen, while a β-carbon is the C-atom adjacent to this central carbon.

The mechanism of E2 reactions is commonly assumed to follow an initial attack of the base to an H-atom. Subsequently, the cleavage of the C_β–H bond leading to XH and the exit of the Y^- leaving group occur in a concerted way, whereby the X–H and C_α–Y bonds are contained in the same plane. This geometry is called coplanar or periplanar configuration. Finally, a double bond is formed between both carbon atoms, which changes the hybridization of the molecular orbitals from sp^3 to

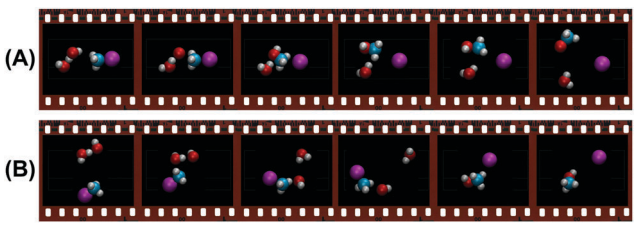

Fig. 13 Exemplary molecular structures along the trajectories of (A) the direct rebound and (B) the indirect mechanism forming the non-solvated S_N2 product ion I^- in the reaction $OH^-(H_2O)$ + CH_3I.[187] The full animations of the trajectories can be found at http://hase-group.ttu.edu/animations.html.

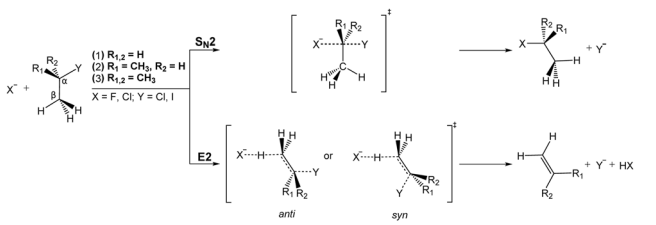

Fig. 14 Schematic representation of S_N2 and E2 reactions. Systems (1)–(3) represent reactions with increasingly substituted haloalkanes, where $R_{1,2}$ denote the substituents. For the S_N2 reaction only the collinear backward approach is shown for simplicity reasons.

sp^2. Base-induced elimination usually occurs *via* a so called *anti*-periplanar geometry, where the X–H and the C–Y bonds lie in the same plane but point in opposite directions. Alternative formation of a *syn*-oriented transition state (same plane and same direction of X–H and C–Y bonds) is also possible and has been found to be thermodynamically stable for several systems.[193]

Due to the fundamental and synthetical relevance of the S_N2/E2 competition, several theoretical and experimental studies have been devoted to understand which physicochemical factors determine the relative efficiency of these pathways. Given the complexity of the systems, density functional theory has been the usual method of choice to study the electronic structure of the stationary points along E2 and S_N2 pathways.[193–197] Based on these calculations, some works have established reaction rates for each process using statistical theories.[198] Other studies based on the activation strain model of chemical reactivity[199] have predicted the dominance of E2 over S_N2 in gas phase reactions of increasing complexity due to a more stabilizing transition state interaction.[196,200]

Many experimental gas-phase studies have been carried out towards providing a direct measure of the branching ratios and a qualitative picture of the effects governing this competition. The challenge of disentangling substitution and elimination products by conventional mass spectrometry is connected to the fact that both reactions generate the same ionic species. Indirect mass spectrometric branching ratios have been deduced by measuring the deuterium kinetic isotope effect (KIE) of reactions with subsequently substituted alkyl halides.[129,201] Experiments have also been attempted to obtain direct branching ratios between both reactions. Brauman and coworkers have measured the reaction rate of S_N2 and E2 in systems where the S_N2 ion–molecule complex undergoes an internal proton transfer.[202] Gronert and coworkers have employed dianions as nucleophiles, therefore producing distinct ionic elimination and substitution products.[126,203,204]

Recently, our group has exploited the capabilities of crossed beam velocity map imaging to disentangle the reaction mechanisms of E2 and S_N2 reactions by monitoring the scattering angle and velocity distribution of product Y^- and correlating them with the respective channels.[205] Several nucleophile-leaving group combinations at stepwise methylated alkyl halides have been investigated,

$$X^- + CH_3Y \xrightarrow{S_N2} Y^- + CH_3X \quad (29)$$

$$X^- + C_2H_5Y \xrightarrow{S_N2} Y^- + C_2H_5X \xrightarrow{E2} Y^- + C_2H_4 + XH \quad (30)$$

$$X^- + {}^iC_3H_7Y \xrightarrow{S_N2} Y^- + {}^iC_3H_7X \xrightarrow{E2} Y^- + C_3H_6 + XH \quad (31)$$

$$X^- + {}^tC_4H_9Y \xrightarrow{S_N2} Y^- + {}^tC_4H_9X \xrightarrow{E2} Y^- + C_4H_8 + XH, \quad (32)$$

with X = (Cl^-, CN^-, F^-) and Y = (Cl^-, I^-). Fig. 15 presents one of such series of measurements for F^- reacting with different alkyl chlorides. A clear transition from direct backward dynamics in F^- + CH_3Cl to forward scattering in F^- + $^iC_3H_7Cl$ and F^- + $^tC_4H_9Cl$ is observed. The product velocity distribution for F^- + C_2H_5Cl presents both reaction mechanisms and represents transition between both mechanistic patterns, which can be extracted in more detail from the product ion scattering angle graph (right panel of Fig. 15). The scattering into the forward hemisphere is observed in all reactions with *tert*-butyl halides, irrespective of the characteristics of nucleophile or leaving group.[205] Given the fact that E2 is assumed to be increasingly favored with methyl substitution on the central carbon atom, we ascribe the observed forward scattered events as direct fingerprints of base induced elimination dynamics.

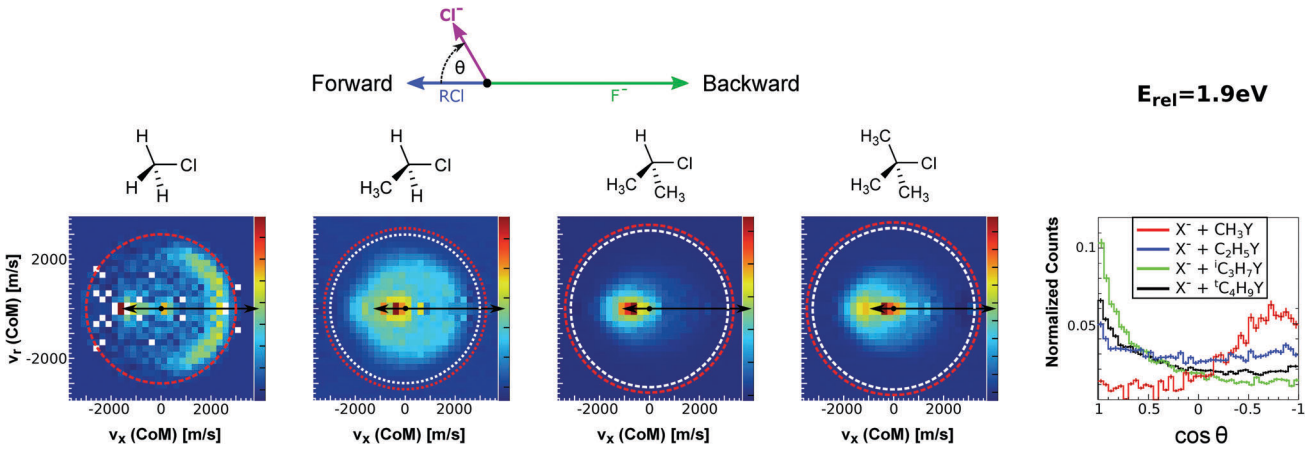

Fig. 15 Center-of-mass velocity distribution and scattering angle of product Cl^- ions produced in the reactions (from left to right) F^- + CH_3Cl, F^- + C_2H_5Cl, F^- + $^iC_3H_7Cl$ and F^- + $^tC_4H_9Cl$. The kinematical limits for the S_N2 and E2 channels are indicated by a red and white circle, respectively. The right panel depicts the resulting Cl^- product scattering angle distributions for the four investigated reactions. The arrows above the images show the relative velocities of the reaction counterparts, as well as the product scattering angle θ. The data are reproduced from ref. 205.

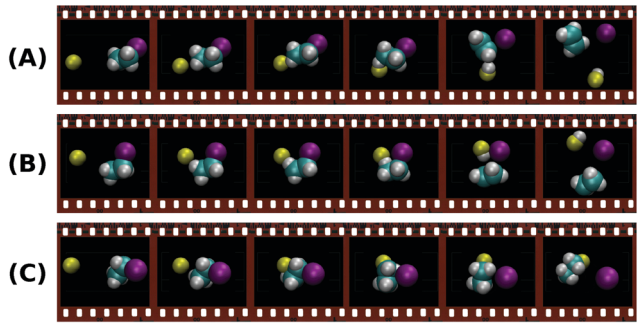

Fig. 16 Snapshots along the most representative reaction trajectories for direct *anti*-E2 (A), direct *syn*-E2 (B) and direct backward S_N2 (C) reactions.[205] The animations of the trajectories can be found at (http://hase-group.ttu.edu/animations.html).

In order to confirm this assignment, the experimental results are supported by electronic structure calculations[206] and classical trajectory simulations on $F^- + C_2H_5I$ at a collision energy of 1.9 eV. While the computed reactive trajectories show several different reaction mechanism, the direct *anti*-periplanar E2 is predicted to be the dominant pathway. Fig. 16 shows exemplary snapshots along the reaction coordinate for the three main mechanisms, direct *anti*-E2, direct *syn*-E2 and direct backward S_N2, all of them occurring over a timescale of several hundred femtoseconds. Further inspection of the reaction probability as a function of impact parameter sheds light into the distinct probability of the direct *anti*-E2 pathway at high impact parameters, in accordance with a stripping-like mechanism leading to forward scattering of the product I^-. This work has provided first evidence of E2-specific mechanistic features. Extraction of quantitative branching ratios between S_N2 and E2 reactions based on the different dynamics is one of the next goals in order to precisely evaluate how steric substitution and relative collision energy affect the competition between these processes. Theoretical efforts towards performing trajectory calculations on similar systems such as $F^- + C_2H_5Cl$ are also underway[207] and will very likely help to further discriminate the distinct dynamics of S_N2 and E2 reactions.

Summary & future directions

Velocity map ion imaging has provided crossed-beam scattering experiments with a great detection technique. Its application to ion–molecule reactive scattering has allowed for numerous studies of cation– and anion–molecule reactions during the last decade. Differential scattering cross sections could be measured for a range of different reactions, from elementary charge transfer and proton transfer to the competition of nucleophilic substitution with base-induced elimination. In many cases state-of-the-art dynamics calculations compare very well with the experiments and have provided valuable insight into the dynamics. Quantum mechanical scattering calculations are, however, still lacking for most ion–molecule reactions.

Many important questions are still unsolved that require further and more advanced scattering experiments. Quantum state-cooling by cryogenic pre-trapping and quantum state-preparation by infrared laser-excitation are two techniques that will allow for improved state-to-state differential scattering and more stringent tests of scattering calculations. In particular, tests of quasiclassical *versus* quantum scattering calculations can be expected from this. Furthermore, quantum-state selection may offer new means to control competing reaction mechanisms, such as S_N2 *versus* E2 reactions.

The dynamics of more complex reactions, *i.e.* reactions involving an increasing number of atoms, can be expected to receive more attention. Possible cases are the formation of long carbon chain molecules, in particular the detected interstellar negative ions, or the observation of ring closure leading to aromatic hydrocarbons. The field of micro-solvation reaction dynamics using crossed-beam imaging has only been started and many aspects of the dynamics are still to be uncovered, such as the role of the cluster temperature or how shell closure around the ion affects the dynamics.

Complexity can also enter *via* the coupling of different electronic hypersurfaces. Charge-transfer and ion-radical reactions are cases that allow to investigate such couplings and possible breakdowns of the Born–Oppenheimer approximation. Coupled potential energy surfaces of different electron spin configuration also influence the dynamics of transition metal ion–molecule reactions. Understanding such reactions is particularly relevant to gain insight into the functioning and the improving of bond activation in catalysis.

Conflicts of interest

There are no conflicts to declare.

Acknowledgements

The authors are very grateful to all their co-workers without whom the described experiments would not have been possible. We also thank our collaboration partners in chemical dynamics theory, in particular Bill Hase and Gábor Czakó. This work was supported by the Austrian Science Fund (FWF), project P25956-N20. E. C. acknowledges support from a DOC-Fellowship by the Austrian Academy of Sciences (ÖAW).

References

1 C.-Y. Ng, *Adv. Chem. Phys.*, 1992, **82**, 401.
2 D. Smith and P. Spanel, *Mass Spectrom. Rev.*, 1995, **14**, 255.
3 A. A. Viggiano, *Phys. Chem. Chem. Phys.*, 2006, **8**, 2557.
4 M. Larsson, W. Geppert and G. Nyman, *Rep. Prog. Phys.*, 2012, **75**, 066901.
5 J. Benedikt, *Int. J. Mod. Phys. D*, 2010, **43**, 043001.
6 E. Herbst, *Philos. Trans. R. Soc., A*, 2000, **358**, 2523–2534.
7 N. de Ruette, K. A. Miller, A. P. O'Connor, X. Urbain, C. F. Buzard, S. Vissapragada and D. W. Savin, *ApJ*, 2016, **816**, 31.
8 P. Ehrenfreund and M. A. Sephton, *Faraday Discuss.*, 2006, **133**, 277–288.

9 J. Mikosch, M. Weidemüller and R. Wester, *Int. Rev. Phys. Chem.*, 2010, **29**, 589–617.
10 M. Langevin, *Ann. Chim. Phys.*, 1905, **5**, 245.
11 R. D. Levine, *Molecular Reaction Dynamics*, Cambridge University Press, 2005.
12 D. K. Böhme, *Int. J. Mass Spectrom.*, 2000, **200**, 97.
13 P. B. Armentrout, *Annu. Rev. Phys. Chem.*, 2001, **52**, 423.
14 I. R. Sims and I. W. M. Smith, *Annu. Rev. Phys. Chem.*, 1995, **46**, 109.
15 R. Wester, *J. Phys. B: At., Mol. Opt. Phys.*, 2009, **42**, 154001.
16 S. Willitsch, *Int. Rev. Phys. Chem.*, 2012, **31**, 175–199.
17 A. T. J. B. Eppink and D. H. Parker, *Rev. Sci. Instrum.*, 1997, **68**, 3477–3484.
18 N. F. Scherer, C. Sipes, R. B. Bernstein and A. H. Zewail, *J. Chem. Phys.*, 1990, **92**, 5239.
19 R. Wester, A. E. Bragg, A. V. Davis and D. M. Neumark, *J. Chem. Phys.*, 2003, **119**, 10032–10039.
20 A. J. Orr-Ewing, *Annu. Rev. Phys. Chem.*, 2015, **66**, 119–141.
21 J. M. Farrar, *Annu. Rev. Phys. Chem.*, 1995, **46**, 525.
22 S. Scherbart and D. Gerlich, *J. Chem. Phys.*, 1989, **90**, 1610.
23 A. Eppink and D. Parker, *J. Chem. Phys.*, 1998, **109**, 4758–4767.
24 A. J. R. Heck and D. W. Chandler, *Annu. Rev. Phys. Chem.*, 1995, **46**, 335.
25 K. Liu, *Annu. Rev. Phys. Chem.*, 2001, **52**, 139.
26 T. N. Kitsopoulos, M. A. Buntine, D. P. Baldwin, R. N. Zare and D. W. Chandler, *Science*, 1993, **260**, 1605.
27 J. J. Lin, J. Zhou, W. Shiu and K. Liu, *Science*, 2003, **300**, 966.
28 B. Zhang, W. Shiu, J. J. Lin and K. Liu, *J. Chem. Phys.*, 2005, **122**, 131102.
29 B. Zhang and K. Liu, *J. Chem. Phys.*, 2005, **122**, 101102.
30 E. L. Reichert, G. Thurau and J. C. Weishaar, *J. Chem. Phys.*, 2002, **117**, 653.
31 J. Mikosch, U. Frühling, S. Trippel, D. Schwalm, M. Weidemüller and R. Wester, *Phys. Chem. Chem. Phys.*, 2006, **8**, 2990–2999.
32 R. Otto, J. Xie, J. Brox, S. Trippel, M. Stei, T. Best, M. R. Siebert, W. L. Hase and R. Wester, *Faraday Discuss.*, 2012, **157**, 41.
33 S. Trippel, M. Stei, R. Otto, P. Hlavenka, J. Mikosch, C. Eichhorn, U. Lourderarj, J. X. Zhang, W. L. Hase, M. Weidemüller and R. Wester, *J. Phys.: Conf. Ser.*, 2009, **194**, 012046.
34 J. Mikosch, J. Zhang, S. Trippel, C. Eichhorn, R. Otto, X. Sun, W. de Jong, M. Weidemüller, W. Hase and R. Wester, *J. Am. Chem. Soc.*, 2013, **135**, 4250.
35 M. Stei, J. von Vangerow, R. Otto, A. H. Kelkar, E. Carrascosa, T. Best and R. Wester, *J. Chem. Phys.*, 2013, **138**, 214201.
36 R. Wester, *Phys. Chem. Chem. Phys.*, 2014, **16**, 396.
37 J. Meyer and R. Wester, *Annu. Rev. Phys. Chem.*, 2017, **68**, 333.
38 L. Pei and J. M. Farrar, *J. Chem. Phys.*, 2012, **136**, 204305.
39 T. Van Voorhis, T. Kowalczyk, B. Kaduk, L.-P. Wang, C.-L. Cheng and Q. Wu, *Annu. Rev. Phys. Chem.*, 2010, **61**, 149–170.
40 S. Falcinelli, P. Candori, F. Pirani and F. Vecchiocattivi, *Phys. Chem. Chem. Phys.*, 2017, **19**, 6933–6944.
41 A. G. G. M. Tielens, *Rev. Mod. Phys.*, 2013, **85**, 1021–1081.
42 W. D. Geppert and M. Larsson, *Chem. Rev.*, 2013, **113**, 8872–8905.
43 J. H. Waite, D. T. Young, T. E. Cravens, A. J. Coates, F. J. Crary, B. Magee and J. Westlake, *Science*, 2007, **316**, 870–875.
44 K. Schowen, H.-H. Limbach, G. Denisov and R. Schowen, *Biochim. Biophys. Acta*, 2000, **1458**, 43–62.
45 J. M. Mayer, *Acc. Chem. Res.*, 2011, **44**, 36–46.
46 P. Tosi, F. Eccher, D. Bassi, F. Pirano, D. Cappelletti and V. Aquilanti, *Phys. Rev. Lett.*, 1991, **67**, 1254–1257.
47 A. W. Kleyn, V. N. Khromov and J. Los, *J. Chem. Phys.*, 1980, **72**, 5282–5283.
48 Y. Huang, C. T. Rettner, D. J. Auerbach and A. M. Wodtke, *Science*, 2000, **290**, 111–114.
49 A. L. Rockwood, S. L. Howard, W.-H. Du, P. Tosi, W. Lindinger and J. H. Futrell, *Chem. Phys. Lett.*, 1985, **114**, 486.
50 K. Birkinshaw, A. Shukla, S. L. Howard and J. H. Futrell, *Chem. Phys.*, 1987, **113**, 149.
51 S. L. Howard, *Chem. Phys. Lett.*, 1990, **178**, 65.
52 R. Candori, S. Cavalli, F. Pirani, A. Volpi, D. Cappelletti, P. Tosi and D. Bassi, *J. Chem. Phys.*, 2001, **115**, 8888.
53 R. Candori, F. Pirani, D. Cappelletti, P. Tosi and D. Bassi, *Int. J. Mass Spectrom.*, 2003, **223**, 499.
54 S. Trippel, M. Stei, J. A. Cox and R. Wester, *Phys. Rev. Lett.*, 2013, **110**, 163201.
55 T. Michaelsen, B. Bastian, E. Carrascosa, J. Meyer, D. H. Parker and R. Wester, *J. Chem. Phys.*, 2017, **147**, 013940.
56 C. â. Liao, R. Xu, S. Nourbakhsh, G. D. Flesch, M. Baer and C. Y. Ng, *J. Chem. Phys.*, 1990, **93**, 4832–4844.
57 G. Gioumousis and D. P. D. P. Stevenson, *J. Chem. Phys.*, 1958, **29**, 294–299.
58 D. P. Stevenson and D. O. Schissler, *J. Chem. Phys.*, 1958, **29**, 282–294.
59 K. Tanaka, J. Durup, T. Kato and I. Koyano, *J. Chem. Phys.*, 1981, **74**, 5561–5571.
60 T. Kato, K. Tanaka and I. Koyano, *J. Chem. Phys.*, 1982, **77**, 834–838.
61 E. A. Gislason and G. Parlant, *J. Chem. Phys.*, 1991, **94**, 6598–6606.
62 M. Hawley and M. A. Smith, *J. Chem. Phys.*, 1992, **96**, 1121.
63 C. Uiterwaal, J. van der Weg, J. van Eck, P. van Emmichoven and A. Niehaus, *Chem. Phys.*, 1996, **209**, 195–203.
64 P. M. Hierl, V. Pacek and Z. Herman, *J. Chem. Phys.*, 1977, **67**, 2678–2686.
65 M. Hernandez-Vera, F. A. Gianturco, R. Wester, H. da Silva Jr, O. Dulieu and S. Schiller, *J. Chem. Phys.*, 2017, **146**, 124310.
66 L. Pei and J. M. Farrar, *J. Chem. Phys.*, 2013, **138**, 124304.
67 L. Pei and J. M. Farrar, *J. Chem. Phys.*, 2012, **137**, 154312.
68 L. Pei and J. M. Farrar, *J. Chem. Phys.*, 2015, **143**, 084304.
69 L. Liu, C. Martin and J. M. Farrar, *J. Chem. Phys.*, 2006, **125**, 133117.
70 L. Liu, Y. Li and J. M. Farrar, *J. Chem. Phys.*, 2006, **124**, 124317.
71 Y. Li and J. M. Farrar, *J. Phys. Chem. A*, 2004, **108**, 9876–9886.
72 Y. Li and J. M. Farrar, *J. Chem. Phys.*, 2004, **120**, 199–205.

73 O. J. Martinez, N. B. Betts, S. M. Villano, N. Eyet, T. P. Snow and V. M. Bierbaum, *ApJ*, 2008, **686**, 1486.
74 D. Edvardsson, P. Baltzer, L. Karlsson, B. Wannberg, D. M. P. Holland, A. D. Shaw and E. E. Rennie, *J. Phys. B: At., Mol. Opt. Phys.*, 1999, **32**, 2583.
75 D. J. Levandier and Y.-H. Chiu, *J. Chem. Phys.*, 2010, **133**, 154304.
76 R. A. Curtis and J. M. Farrar, *J. Chem. Phys.*, 1986, **84**, 127–134.
77 E. Roueff and E. Herbst, *J. Phys.: Conf. Ser.*, 2009, **192**, 012008.
78 E. F. van Dishoeck, *Faraday Discuss.*, 2014, **168**, 9–47.
79 D. Buhl and L. E. Snyder, *Nature*, 1970, **228**, 267.
80 R. C. Woods, C. S. Gudeman, R. F. Goldsmith, G. R. Huguenin, W. M. Irvine, A. Hjalmarson, L.-A. Nyman and H. Olofsson, *Astrophys. J.*, 1983, **270**, 583–588.
81 L. M. Ziurys and A. J. Apponi, *Ap. J. Lett.*, 1995, **455**, L73.
82 A. J. Apponi and L. M. Ziurys, *Astrophys. J.*, 1997, **481**, 800–808.
83 T. Li, H. Hirano, T. Amano and R. J. Le Roy, *J. Phys. Chem.*, 2008, **129**, 244306.
84 S. J. Klippenstein, Y. Georgievskii and B. J. McCall, *J. Phys. Chem. A*, 2010, **114**, 278–290.
85 M. A. Smith, S. Schlemmer, J. von Richthofen and D. Gerlich, *ApJ*, 2002, **578**, 87–90.
86 M. Mladenovic and S. Schmatz, *J. Chem. Phys.*, 1998, **109**, 4456–4470.
87 E. Carrascosa, M. Stei, M. A. Kainz and R. Wester, *Mol. Phys.*, 2015, **113**, 3955.
88 E. Carrascosa, M. A. Kainz, M. Stei and R. Wester, *J. Phys. Chem. Lett.*, 2016, **7**, 2742–2747.
89 K. R. Redeker, N.-Y. Wang, J. C. Low, A. McMillan, S. C. Tyler and R. J. Cicerone, *Science*, 2000, **290**, 966–969.
90 R. C. Rhew, *J. Geophys. Res.*, 2011, **116**, G03026.
91 L. Pei and J. M. Farrar, *J. Phys. Chem. A*, 2016, **120**, 6122–6128.
92 C. M. Nichols, Z. Yang, B. B. Worker, D. R. Hager, N. M. M. Nibbering and V. M. Bierbaum, *Phys. Chem. Chem. Phys.*, 2013, **15**, 561–567.
93 Z. Herman, J. H. Futrell and B. Friedrich, *Int. J. Mass Spectrom. Ion Processes*, 1984, **58**, 181.
94 A. K. Shukla, K. Qian, S. L. Howard, S. G. Anderson, K. W. Sohlberg and J. H. Futrell, *Int. J. Mass Spectrom. Ion Processes*, 1989, **92**, 147–169.
95 A. K. Shukla, K. Qian, S. Anderson and J. H. Futrell, *J. Am. Soc. Mass Spectrom.*, 1990, **1**, 6.
96 L. Pei and J. M. Farrar, *Int. J. Mass Spectrom.*, 2015, **377**, 93–100.
97 M. K. Bullitt, C. H. Fisher and J. L. Kinsey, *J. Chem. Phys.*, 1974, **60**, 478–491.
98 H. Schwarz, *Angew. Chem.*, 1991, **103**, 837–838.
99 J. Roithova and D. Schroeder, *Chem. Rev.*, 2010, **110**, 1170–1211.
100 P. B. Armentrout, *Science*, 1991, **251**, 175–179.
101 S. S. Yi, M. R. A. Blomberg, P. E. M. Siegbahn and J. C. Weisshaar, *J. Phys. Chem. A*, 1998, **102**, 395–411.
102 M. Blomberg, S. S. Yi, R. J. Noll and J. C. Weisshaar, *J. Phys. Chem. A*, 1999, **103**, 7254–7267.
103 S. S. Yi, E. L. Reichert and J. C. Weisshaar, *Int. J. Mass Spectrom.*, 1999, **185-187**, 837–846.
104 R. J. Noll, S. S. Yi and J. C. Weisshaar, *J. Phys. Chem. A*, 1998, **102**, 386–394.
105 E. L. Reichert, S. S. Yi and J. C. Weisshaar, *Int. J. Mass Spectrom.*, 2000, **195/196**, 55–69.
106 E. L. Reichert, G. Thurau and J. C. Weishaar, *J. Phys. Chem. A*, 2002, **106**, 5563.
107 S. S. Yi, E. L. Reichert, M. C. Holthausen, W. Koch and J. C. Weisshaar, *Chem. – Eur. J.*, 2000, **6**, 2232–2245.
108 J. Sugar and C. Corliss, *J. Phys. Chem. Ref. Data*, 1985, **14**(Suppl. 2), 644.
109 P. A. M. Van Koppen, P. R. Kemper and M. T. Bowers, *J. Am. Chem. Soc.*, 1992, **114**, 10941–10950.
110 P. M. van Koppen, M. T. Bowers, E. R. Fisher and P. B. Armentrout, *J. Am. Chem. Soc.*, 1994, **116**, 3780–3791.
111 P. A. M. Van Koppen, J. Brodbelt-Lustig, M. T. Bowers, D. V. Dearden, J. L. Beauchamp, E. R. Fisher and P. B. Armentrout, *J. Am. Chem. Soc.*, 1991, **113**, 2359–2369.
112 M. A. Hanratty, J. L. Beauchamp, A. J. Illies and M. T. Bowers, *J. Am. Chem. Soc.*, 1985, **107**, 1788–1789.
113 M. A. Hanratty, J. L. Beauchamp, A. J. Illies, P. Van Koppen and M. T. Bowers, *J. Am. Chem. Soc.*, 1988, **110**, 1–14.
114 P. Pechukas, J. C. Light and C. Rankin, *J. Chem. Phys.*, 1966, **44**, 794.
115 L. Pei, E. Carrascosa, N. Yang, S. Falcinelli and J. M. Farrar, *J. Phys. Chem. Lett.*, 2015, **6**, 1684–1689.
116 A. Cunje, C. F. Rodriquez, M. H. Lien and A. C. Hopkinson, *J. Org. Chem.*, 1996, **61**, 5212.
117 M. C. McCarthy, C. A. Gottlieb, H. Gupta and P. Thaddeus, *Ap. J. Lett.*, 2006, **652**, 141.
118 P. Thaddeus, C. A. Gottlieb, H. Gupta, S. Brünken, M. C. McCarthy, M. Agundez, M. Guelin and J. Cernicharo, *ApJ*, 2008, **677**, 1132.
119 S. Schlemmer, W. Geppert, A. Wolf, J. Glosik, D. Parker, L. Wiesenfeld, H. Kreckel, D. W. Savin and O. Asvany, *Gas Phase Chemistry*, Wiley-VCH Verlag GmbH & Co., KGaA, 2014, pp. 109–228.
120 R. C. Fortenberry, *J. Phys. Chem. A*, 2015, **119**, 9941–9953.
121 M. B. Smith and J. March, *March's Advanced Organic Chemistry: Reactions, Mechanisms and Structure*, John Wiley & Sons, 2007.
122 P. Walden, *Ber. Dtsch. Chem. Ges.*, 1896, **29**, 133–138.
123 E. D. Hughes and C. K. Ingold, *J. Chem. Soc.*, 1935, 244–255.
124 A. A. Viggiano, R. A. Morris, J. S. Paschkewitz and J. F. Paulson, *J. Am. Chem. Soc.*, 1992, **114**, 10477–10482.
125 W. L. Hase, *Science*, 1994, **266**, 998–1002.
126 A. E. Flores and S. Gronert, *J. Am. Chem. Soc.*, 1999, **121**, 2627–2628.
127 J. K. Laerdahl and E. Uggerud, *Int. J. Mass Spectrom.*, 2002, **214**, 277–314.
128 G. Vayner, K. N. Houk, W. L. Jorgensen and J. I. Brauman, *J. Am. Chem. Soc.*, 2004, **126**, 9054–9058.
129 J. Garver, N. Eyet, S. Villano, Y. Zhibo and V. Bierbaum, *Int. J. Mass Spectrom.*, 2011, **301**, 151–158.

130 J. Xie and W. L. Hase, *Science*, 2016, **352**, 32–33.
131 J. M. Garver, Y. R. Fang, N. Eyet, S. M. Villano, V. M. Bierbaum and K. C. Westaway, *J. Am. Chem. Soc.*, 2010, **132**, 3808–3814.
132 A. J. Orr-Ewing, *J. Chem. Phys.*, 2014, **140**, 090901.
133 M. L. Chabinyc, S. L. Craig, C. K. Regan and J. I. Brauman, *Science*, 1998, **279**, 1882–1886.
134 W. Olmstead and J. Brauman, *J. Am. Chem. Soc.*, 1977, **99**, 4219.
135 W. L. Hase and Y. J. Cho, *J. Chem. Phys.*, 1993, **98**, 8626–8639.
136 L. Sun, K. Song and W. L. Hase, *Science*, 2002, **296**, 875–878.
137 S. T. Graul and M. T. Bowers, *J. Am. Chem. Soc.*, 1994, **116**, 3875–3883.
138 Y. Wang, H. Song, I. Szabo, G. Czako, H. Guo and M. Yang, *J. Phys. Chem. Lett.*, 2016, **7**, 3322–3327.
139 A. P. Bento and F. M. Bickelhaupt, *J. Org. Chem.*, 2008, **73**, 7290–7299.
140 I. Fernandez and F. M. Bickelhaupt, *Chem. Soc. Rev.*, 2014, **43**, 4953–4967.
141 M. N. Glukhovtsev, A. Pross and L. Radom, *J. Am. Chem. Soc.*, 1996, **118**, 6273–6284.
142 L. A. Angel and K. M. Ervin, *J. Phys. Chem. A*, 2001, **105**, 4042–4051.
143 M. Stei, E. Carrascosa, M. A. Kainz, A. Kelkar, J. Meyer, I. Szabo, G. Czako and R. Wester, *Nat. Chem.*, 2016, **8**, 151.
144 J. Mikosch, S. Trippel, C. Eichhorn, R. Otto, U. Lourderaj, J. X. Zhang, W. L. Hase, M. Weidemüller and R. Wester, *Science*, 2008, **319**, 183.
145 R. Otto, J. Brox, S. Trippel, M. Stei, T. Best and R. Wester, *Nat. Chem.*, 2012, **4**, 534–538.
146 E. Carrascosa, M. Bawart, M. Stei, F. Linden, F. Carelli, J. Meyer, W. D. Geppert, F. A. Gianturco and R. Wester, *J. Chem. Phys.*, 2015, **143**, 184309.
147 U. Lourderaj, R. Sun, S. C. Kohale, G. L. Barnes, W. A. de Jong, T. L. Windus and W. L. Hase, *Comput. Phys. Commun.*, 2014, **185**, 1074–1080.
148 I. Szabó, A. G. Császár and G. Czakó, *Chem. Sci.*, 2013, **4**, 4362.
149 I. Szabó, H. Telekes and G. Czakó, *J. Chem. Phys.*, 2015, **142**, 244301.
150 J. Xie, R. Otto, J. Mikosch, J. Zhang, R. Wester and W. L. Hase, *Acc. Chem. Res.*, 2014, **47**, 2960.
151 I. Szabó and G. Czakó, *Nat. Commun.*, 2015, **6**, 5972.
152 J. Zhang, J. Mikosch, S. Trippel, R. Otto, M. Weidemüller, R. Wester and W. L. Hase, *J. Phys. Chem. Lett.*, 2010, **1**, 2747–2752.
153 J. Zhang, U. Lourderaj, R. Sun, J. Mikosch, R. Wester and W. L. Hase, *J. Chem. Phys.*, 2013, **138**, 114309.
154 T. Su, H. Wang and W. L. Hase, *J. Phys. Chem. A*, 1998, **102**, 9819–9828.
155 J.-L. Le Garrec, B. R. Rowe, J. L. Queffelec, J. B. A. Mitchell and D. C. Clary, *J. Chem. Phys.*, 1997, **107**, 1021–1024.
156 L. A. Angel and K. M. Ervin, *J. Am. Chem. Soc.*, 2003, **125**, 1014–1027.
157 J. Xie, R. Sun, M. Siebert, R. Otto, R. Wester and W. L. Hase, *J. Phys. Chem. A*, 2013, **117**, 7162.
158 R. Sun, J. Xie, J. Zhang and W. L. Hase, *Int. J. Mass Spectrom.*, 2015, **377**, 222–227.
159 I. Szabó, B. Olasz and G. Czakó, *J. Phys. Chem. Lett.*, 2017, **8**, 2917–2923.
160 R. A. Morris and A. A. Viggiano, *J. Phys. Chem.*, 1994, **98**, 3740–3746.
161 D. M. Cyr, M. G. Scarton, K. B. Wiberg, M. A. Johnson, S. Nonose, J. Hirokawa, H. Tanaka, T. Kondow and R. A. Morris, *J. Am. Chem. Soc.*, 1995, **117**, 1828–1832.
162 L. A. Angel and K. M. Ervin, *J. Phys. Chem. A*, 2004, **108**, 9827–9833.
163 J. Xie, S. C. Kohale, W. L. Hase, S. G. Ard, J. J. Melko, N. S. Shuman and A. A. Viggiano, *J. Phys. Chem. A*, 2013, **117**, 14019.
164 J. Zhang, J. Xie and W. L. Hase, *J. Phys. Chem. A*, 2015, **119**, 12517–12525.
165 B. Olasz, I. Szabó and G. Czakó, *Chem. Sci.*, 2017, **8**, 3164–3170.
166 E. Carrascosa, T. Michaelsen, M. Stei, B. Bastian, J. Meyer, J. Mikosch and R. Wester, *J. Phys. Chem. A*, 2016, **120**, 4711.
167 J. Chandrasekhar, S. F. Smith and W. L. Jorgensen, *J. Am. Chem. Soc.*, 1984, **106**, 3049.
168 D. L. Thomsen, J. N. Reece, C. M. Nichols, S. Hammerum and V. M. Bierbaum, *J. Am. Chem. Soc.*, 2013, **135**, 15508–15514.
169 D. K. Bohme and G. I. Mackay, *J. Am. Chem. Soc.*, 1981, **103**, 978–979.
170 P. M. Hierl, A. F. Ahrens, M. Henchman, A. A. Viggiano, J. F. Paulson and D. C. Clary, *J. Am. Chem. Soc.*, 1986, **108**, 3140–3142.
171 P. M. Hierl, A. F. Ahrens, M. J. Henchman, A. A. Viggiano, J. F. Paulson and D. C. Clary, *Faraday Discuss.*, 1988, **85**, 37–51.
172 A. A. Viggiano, S. T. Arnold, R. A. Morris, A. F. Ahrens and P. M. Hierl, *J. Phys. Chem.*, 1996, **100**, 14397–14402.
173 X. Liu, J. Xie, J. Zhang, L. Yang and W. L. Hase, *J. Phys. Chem. Lett.*, 2017, **8**, 1885–1892.
174 L. Yang, X. Liu, J. Zhang and J. Xie, *Phys. Chem. Chem. Phys.*, 2017, **19**, 9992–9999.
175 J. V. Seeley, R. A. Morris, A. A. Viggiano, H. B. Wang and W. L. Hase, *J. Am. Chem. Soc.*, 1997, **119**, 577–584.
176 J. V. Seeley, R. A. Morris and A. A. Viggiano, *J. Phys. Chem. A*, 1997, **101**, 4598–4601.
177 S. Raugei, G. Cardini and V. Schettino, *J. Chem. Phys.*, 2001, **114**, 4089–4098.
178 H. Tachikawa, M. Igarashi and T. Ishibashi, *Chem. Phys. Lett.*, 2002, **363**, 355–361.
179 H. Tachikawa, *J. Chem. Phys.*, 2006, **125**, 133119.
180 I. Adamovic and M. S. Gordon, *J. Phys. Chem. A*, 2005, **109**, 1629–1636.
181 J. Zhang, L. Yang and L. Sheng, *J. Phys. Chem. A*, 2016, **120**, 3613–3622.
182 C. K. Regan, S. L. Craig and J. I. Brauman, *Science*, 2002, **295**, 2245.
183 R. A. J. O'Hair, G. E. Davico, J. Hacaloglu, T. T. Dang, C. H. DePuy and V. M. Bierbaum, *J. Am. Chem. Soc.*, 1994, **116**, 3609–3610.

184 W.-P. Hu and D. G. Truhlar, *J. Am. Chem. Soc.*, 1994, **116**, 7797.
185 K. Doi, E. Togano, S. S. Xantheas, R. Nakanishi, T. Nagata, T. Ebata and Y. Inokuchi, *Angew. Chem., Int. Ed.*, 2013, **52**, 4380.
186 R. Otto, J. Brox, M. Stei, S. Trippel, T. Best and R. Wester, *Nat. Chem.*, 2012, **4**, 534–538.
187 J. Xie, R. Otto, R. Wester and W. L. Hase, *J. Chem. Phys.*, 2015, **142**, 244308.
188 J. Xie, M. J. Scott, W. L. Hase, P. M. Hierl and A. A. Viggiano, *Z. Phys. Chem.*, 2015, **229**, 1747–1763.
189 R. Otto, J. Brox, S. Trippel, M. Stei, T. Best and R. Wester, *J. Phys. Chem. A*, 2013, **117**, 8139.
190 J. Xie, M. McCellan, R. Sun, S. C. Kohale, N. Govind and W. L. Hase, *J. Phys. Chem. A*, 2015, **119**, 817–825.
191 J. Xie, X. Ma, J. Zhang, P. M. Hierl, A. A. Viggiano and W. L. Hase, *Int. J. Mass Spectrom.*, 2017, **418**, 122–129.
192 J. Zhang, L. Yang, J. Xie and W. L. Hase, *J. Phys. Chem. Lett.*, 2016, **7**, 660.
193 F. M. Bickelhaupt, E. J. Baerends, N. M. M. Nibbering and T. Ziegler, *J. Am. Chem. Soc.*, 1993, **115**, 9160–9173.
194 S. Gronert, *J. Am. Chem. Soc.*, 1993, **115**, 652–659.
195 P. Bento, M. Sola and F. M. Bickelhaupt, *J. Chem. Theory Comput.*, 2008, **4**, 929–940.
196 X. Wu, X. Sun, X. Wei, Y. Ren, N. Wong and W. Li, *J. Chem. Theory Comput.*, 2009, **5**, 1597–1606.
197 Y. Zhao and D. G. Truhlar, *J. Chem. Theory Comput.*, 2010, **6**, 1104–1108.
198 W.-P. Hu and D. G. Truhlar, *J. Am. Chem. Soc.*, 1996, **118**, 860–869.
199 F. M. Bickelhaupt, *J. Comput. Chem.*, 1999, **20**, 114–128.
200 L. P. Wolters, Y. Ren and F. M. Bickelhaupt, *ChemistryOpen*, 2014, **3**, 29–36.
201 S. M. Villano, S. Kato and V. M. Bierbaum, *J. Am. Chem. Soc.*, 2006, **128**, 736–737.
202 B. D. Wladkowski and J. I. Brauman, *J. Am. Chem. Soc.*, 1992, **114**, 10643–10644.
203 C. H. DePuy, S. Gronert, A. Mullin and V. M. Bierbaum, *J. Am. Chem. Soc.*, 1990, **112**, 8650–8655.
204 S. Gronert, A. E. Fagin and L. Wong, *J. Am. Chem. Soc.*, 2007, **129**, 5330–5331.
205 E. Carrascosa, J. Meyer, J. Zhang, M. Stei, T. Michaelsen, W. L. Hase, L. Yang and R. Wester, *Nat. Commun.*, 2017, **8**, 25.
206 L. Yang, J. Zhang, J. Xie and C. Zhao, *J. Phys. Chem. A*, 2017, **121**, 1078–1085.
207 V. Tajti and G. Czako, *J. Phys. Chem. A*, 2017, **121**, 2847.

